Master's Thesis
석사 학위논문

Study of Hybrid Photocatalytic System for CO_2 Reduction into Hydrocarbon Fuels under Solar Irradiation

Seung-Min Park (박 승 민 朴 承 珉)

Department of Energy Systems Engineering
에너지시스템공학전공

DGIST

2015

Master's Thesis
석사 학위논문

Study of Hybrid Photocatalytic System for CO_2 Reduction into Hydrocarbon Fuels under Solar Irradiation

Seung-Min Park (박 승 민 朴 承 珉)

Department of Energy Systems Engineering
에너지시스템공학전공

DGIST

2015

Study of Hybrid Photocatalytic system for CO_2 Reduction into Hydrocarbon Fuels under Solar Irradiation

Advisor : Professor Su-Il In

Co-advisor : Ph.D Yiseul Park

by

Seung-Min Park

Department of Energy Systems Engineering

DGIST

A thesis submitted to the faculty of DGIST in partial fulfillment of the requirements for the degree of Master of Science in the Department of Energy Systems Engineering. The study was conducted in accordance with Code of Research Ethics[1]

01. 09. 2014

Approved by

Professor Su-Il In _____ (Signature)
(Advisor)

Ph.D Yiseul Park _____ (Signature)
(Co-advisor)

[1] Declaration of Ethical Conduct in Research: I, as a graduate student of DGIST, hereby declare that I have not committed any acts that may damage the credibility of my research. These include, but are not limited to: falsification, thesis written by someone else, distortion of research findings or plagiarism. I affirm that my thesis contains honest conclusions based on my own careful research under the guidance of my thesis adVisor.

Study of Hybrid Photocatalytic System for CO_2 Reduction into Hydrocarbon Fuels under Solar Irradiation

Seung-Min Park

Accepted in partial fulfillment of the requirements for the degree of
Master of Science.

01. 09. 2014

Head of Committee _____(인)
Prof. Su-Il In

Committee Member _____(인)
Ph.D Yiseul Park

Committee Member _____(인)
Ph.D Soo-Keun Lee

MS/ES

201324005

박 승 민. Seung-Min Park. Study of Hybrid Photocatalytic System for CO_2 Reduction into Hydrocarbon Fuels under Solar Irradiation. Department of Energy Systems Engineering. 2015. 57p. Advisors Prof. Su-Il, In. Co-advisors Dr. Yiseul Park.

Abstract

Recently, the needs for sustainable energy are increased with the energy shortage and environmental pollution. The research on photocatalytic CO_2 reduction is one of the promising research fields to address these needs. In this study, a hybrid photocatalytic system for CO_2 reduction into hydrocarbon fuels was researched to enhance CO_2 reduction efficiency by semiconductor nanoparticles and titanate (TiO_2).

One is that C, N co-doped sodium titanate nanotube (C, N-TNT) was synthesized by a hydrothermal method and calcination treatment. The photocatalytic activities of C, N-TNT were evaluated by methylene blue degradation and CO_2 reduction to hydrocarbon fuel under simulated solar light irradiation. The C,N-TNT1 (Urea/TiO_2 =10) showed highest degradation rate for photocatalytic dye degradation. On the other hand, it showed highest CH_4 production rate for C, N-TNT06.

Another is that hybrid CuO-$TiO_{2-x}Cl_x$ heterostructured composites was prepared by a novel synthetic method and its photocatalytic activity was evaluated with CO_2 reduction by gas chromatogram (GC). A strategy to enhance the CO_2 reduction efficiency is to couple CuO with Cl doped TiO_2 to form p-n heterojunction that can enhance a charge separation of the photo-generated charge carriers. CT07 shows the dramatically enhanced CO_2 reduction activity.

Keyword: C,N-TNT, Chlorine doped TiO_2, copper oxide, p-n heterojunction, photocatalytic CO_2 reduction,

List of Contents

List of Figures

1. Scope and Organization of the Thesis

This thesis describes the use of quantum nanoparticles and modified titania (TiO_2) as photocatalysts for the photocatalytic reduction of carbon dioxide (CO_2) into solar fuels under simulated solar irradiation. It has focused on the photocatalytic CO_2 reduction by different types of photocatalytic systems having unique non-metal co-doped structure and p-n heterojunction structure.

In the first section, the photocatalytic activities of carbon and nitrogen co-doped sodium titanate nanotube (C, N co-doped TNT) will be estimated by photocatalytic CO_2 reduction and dye degradation. Second, a copper @ cupric oxide ($Cu@Cu_2O$) core-shell nanoparticles and $CuO\text{-}TiO_{2-x}Cl_x$ heterostructured composites will be discussed to realize p-n heterojunction between p-type semiconductor and chlorine doped titanate by a novel synthetic method. A gas chromatogram (GC) which can detect the organic molecules such as methane, ethane *etc.*, will be introduced to evaluate the photocatalytic activity under the simulated solar light.

In a final section, all of contents will be summarized to explain the advantages and creativity for these experiments and will propose the prospects of solar light sensitive photocatalysts in the future.

2. Introduction

2.1 Research Background

Recently, hydrocarbon fuels are the most important energy source for human community with their stability and high energy density (33 GJ/m^3 for gasoline).[1] Due to these advantages of hydrocarbon fossil fuels such as coal, crude oil and shale gas, the energy demand in the earth is also dramatically increasing with the development of technology. These phenomena induce the shortage and restriction on the hydrocarbon fossil fuels. Owing to the indiscreet use of fossil fuel, Atmospheric carbon dioxide concentration is continue to rise for the foreseeable future from ongoing burning of fossil fuels. The world CO_2 emission and global temperature rising from 1965 to 2014 is shown in Figure 2.1.[2] The trend of CO_2 emission is proportional to that of global temperature rise. Total CO_2 emission at 2014 is about 3 times higher than that of 1965. Global temperature is also rising with the amount of CO_2 emission. In addition, it is reported that the world consumes approximately 1 billion barrels of fossil fuels at every each 12 days, corresponds to atmospheric release of 1 trillion pounds of CO_2.[3] Therefore the continuous rise in CO_2 emission is considered to be a great factor

for artificial climate change or greenhouse effect. These concerns have emphasized the warning of environmental problems and the need to develop renewable energy resource. So the remedy to solve these concerns have been studied intensively. However the process to treat CO_2 generally needs substantial energy input.

Sunlight is a one of the best candidates to address these problems. It provides an infinite energy source to human being. The solar light energy reaching on the Earth in one hour is corresponding with the annual global energy consumption.[4] It means that only converting about 10 % of the solar energy on 0.3 % of the surface of the planet would enough to exceed the energy need in 2050.[5] Harvesting the solar energy and its storage in the chemical bond is a promising technique to address the energy demand in the current and future. Solar fuels, which are high energy compound such as methane, ethane or methanol generated by solar light can be used as an energy source. Catalyst that converts CO_2 into hydrocarbon fuels by sunlight is innovative to solve these problems due to generate solar fuel with no energy consumption.

The ideas that chemical conversion of CO_2 into hydrocarbon fuels have been many attention for more than 30 years, including thermochemical conversion, biological conversion, electrochemical conversion, and photocatalytic conversion to activate the very stable carbon dioxide molecule.

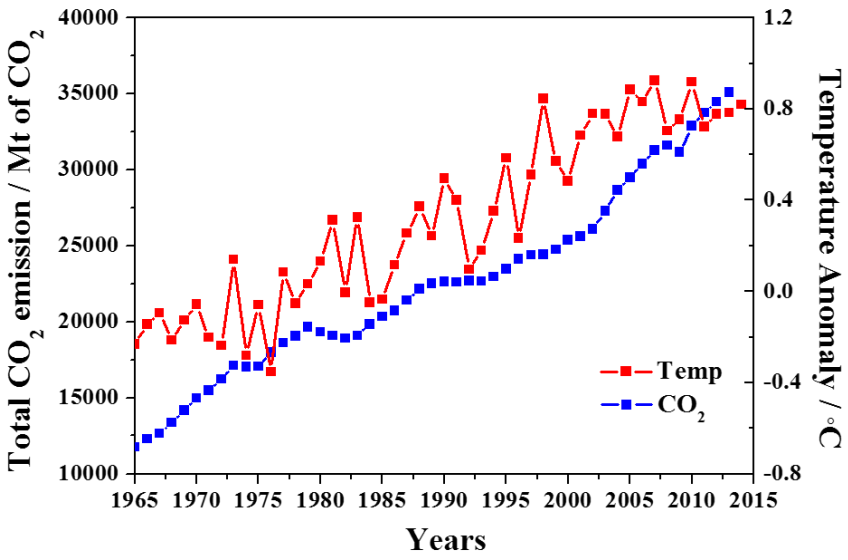

Figure 2. 1 The world CO_2 emission and global temperature rising from 1965 to 2014.

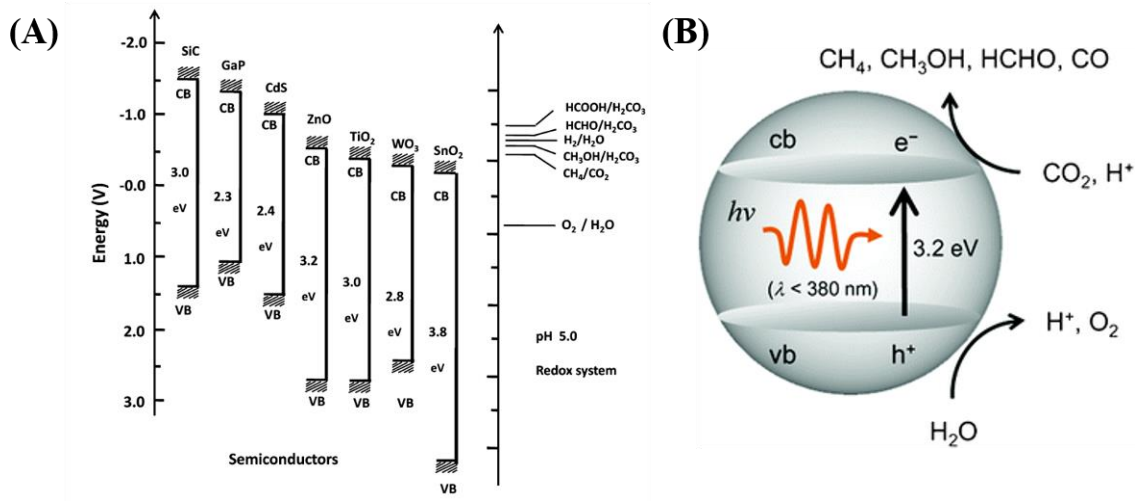

Figure 2. 2 (A) Band position of the semiconductor photocatalysts relative to energy level of the redox couple in water from Ref. 6. (B) Reaction scheme of photocatalytic CO_2 reduction with H_2O on TiO_2 photocatalyst from Ref. 7.

In particular, the photocatalytic CO_2 reduction into hydrocarbon fuels is a challenging to substitute conventional fossil fuels with advantages as follows i) this reaction can be carried out in relatively mild condition such as room temperature and pressure; ii) CO_2 molecules as an energy source is very abundant in the Earth; iii) the photocatalytic CO_2 reduction can directly generate short chain hydrocarbon fuel such as methane (CH_4), methanol (CH_3OH), ethane (C_2H_6) and so on, which can replace fossil fuels in energy crisis by CO_2 as a carbon source in chemical industry.

In spite of theses advantage of the photocatalytic CO_2 reduction, almost research are still in the experimental stage due to the drawbacks of low photoconversion efficiency and selectivity. Many design strategies are introduced to overcome the reactant adsorption, charge separation, light harvesting, and CO_2 activation. The reaction of photocatalytic methane production generally requires eight electrons generated by photons. To produce significant amounts of hydrocarbon, an efficient photocatalysts that can use maximum solar energy are needed. Figure 2.2 shows the band edge position of the different semiconductor photocatalysts with the energy level of the redox couple of different chemical species by CO_2[6] and the primary catalytic process in TiO_2[7]. TiO_2 and ZnO are good candidates for CO_2 reduction due to CH_4/CO_2 redox energy level lies on the conduction band of the semiconductor. For the simple mechanism of CO_2 reduction, the electrons and holes produced by UV irradiation in the semiconductor nanoparticles are participated in the reduction of CO_2 at

the conduction band and the oxidation of hole scavenger at valence band. The holes from the valence band do the process of the oxidation and produced protons (H^+). The protons and CO_2 adsorbed on the surface of the catalyst are participated in the reduction reaction by photogenerated electrons to produce hydrocarbon fuels.

In 1979, Inoue and Honda *et al.*[8] described the photocatalytic CO_2 conversion system to generate organic fuels such as methanol, methane, formaldehyde, and formic acid by using the mixture of suspended oxide and non-oxide semiconductor particles. They suggested that conversion of CO_2 into methane was a multistep process related to multi electrons.

$$H_2O + 2h^+ \rightarrow {}^1/_2\ O_2 + 2H^+ \quad (1)$$

$$CO_2(aq.) + 2H^+ + 2e^- \rightarrow HCOOH \quad (2)$$

$$HCOOH + 2H^+ + 2e^- \rightarrow HCHO + H_2O \quad (3)$$

$$HCHO + 2H^+ + 2e^- \rightarrow CH_3OH \quad (4)$$

$$CH_3OH + 2H^+ + 2e^- \rightarrow CH_4 + H_2O \quad (5)$$

Grätzel and co-workers[9] reported the generation of methane by Ru/RuO_x sensitized TiO_2 as a catalyst under carbon dioxide and hydrogen atmosphere. The reaction rate of methane generation is sharply increased through the carbidic (Ru-C) surface carbon on Ru as well as photo-excitation of Ru/RuO_x supported TiO_2 system under UV light illumination. In the photocatalytic CO_2 reduction reaction, the key issue is the enhancement of conversion efficiency by the surface modification of photocatalysts to increase the charge separation rate, light harvesting, selectivity and adsorption ability of CO_2 molecule. Therefore, this thesis focuses on the surface modification of TiO_2 by p-n heterojunction with CuO, non-metal such as C, N and Cl doping, and narrow bandgap semiconductor quantum dot sensitized system to enhance these factors.

2.2 References

1. Energy Information Administration (EIA). Annual Energy Review 2008, *Annual Energy Review* [Online], **2008**. (accessed www.eia.doe.gov/aer).
2. British Petroleum. BP Statistical Review of World Energy June 2014, *The Statistical Review* [Online], **2014**. (accessed www.bp.com/statisticalreview).
3. Varghese, O. K.; Paulose, M.; LaTempa, T. J.; Grimes, C. A., High-Rate Solar Photocatalytic Conversion of CO_2 and Water Vapor to Hydrocarbon Fuels. *Nano Letters* **2009,** *9* (2), 731-737.
4. Lewis, N. S.; Nocera, D. G., Powering the planet: Chemical challenges in solar energy utilization. *Proceedings of the National Academy of Sciences* **2006,** *103* (43), 15729-15735.
5. Habisreutinger, S. N.; Schmidt-Mende, L.; Stolarczyk, J. K., Photocatalytic Reduction of CO_2 on TiO_2 and Other Semiconductors. *Angewandte Chemie International Edition* **2013,** *52* (29), 7372-7408.
6. Roy, S. C.; Varghese, O. K.; Paulose, M.; Grimes, C. A., Toward Solar Fuels: Photocatalytic Conversion of Carbon Dioxide to Hydrocarbons. *ACS Nano* **2010,** *4* (3), 1259-1278.
7. Mori, K.; Yamashita, H.; Anpo, M., Photocatalytic reduction of CO_2 with H_2O on various titanium oxide photocatalysts. *RSC Advances* **2012,** *2* (8), 3165-3172.
8. Inoue, T.; Fujishima, A.; Konishi, S.; Honda, K., Photoelectrocatalytic reduction of carbon dioxide in aqueous suspensions of semiconductor powders. *Nature* **1979,** *277* (5698), 637-638.
9. Thampi, K. R.; Kiwi, J.; Gratzel, M., Methanation and photo-methanation of carbon dioxide at room temperature and atmospheric pressure. *Nature* **1987,** *327* (6122), 506-508.

3. Equipment

3.1 UV-Visible-Near Intrared absorption spectroscopy (UV-Vis-NIR)

Ultraviolet–Visible spectroscopy (UV-Vis) refers to absorption spectroscopy or reflectance spectroscopy in the ultraviolet-Visible spectral region. Figure 3.1A shows the schematic illustration of UV-Visible spectrometer operation. For double-beam UV-Vis spectrometer, the light from D_2 and tungsten lamp is split two beams for the analysis. One is used for reference, the other passes through the samples and the result display the ratio of the two beam intensities.[1] Figure 3.2B indicates various electronic transitions in molecular energy level by light absorption. There are three kinds of electrons in molecules: namely σ (single bond), π (multiple bond) or n (non-bonding). i) σ bond electrons are most stable due to have lowest energy. It requires a lot of energy (UV region) to excite to a higher energy level. ii) π bond electrons have much higher energy than the ground state. So these electrons can be excited more easily with lower energy (UV or Vis). iii) n bonding electrons are generally related to the lone pair electrons.[2] These have higher energy than π-electrons and can be excited by UV or Visible light. When the molecules absorb the light energy, the electrons get excited to lowest unoccupied molecular orbital (LUMO, anti-bonding) from the highest occupied molecular orbital (HOMO, bonding or non-bonding energy level). The difference between HOMO and LUMO is called energy gap or band gap which is a characteristic value for each material.

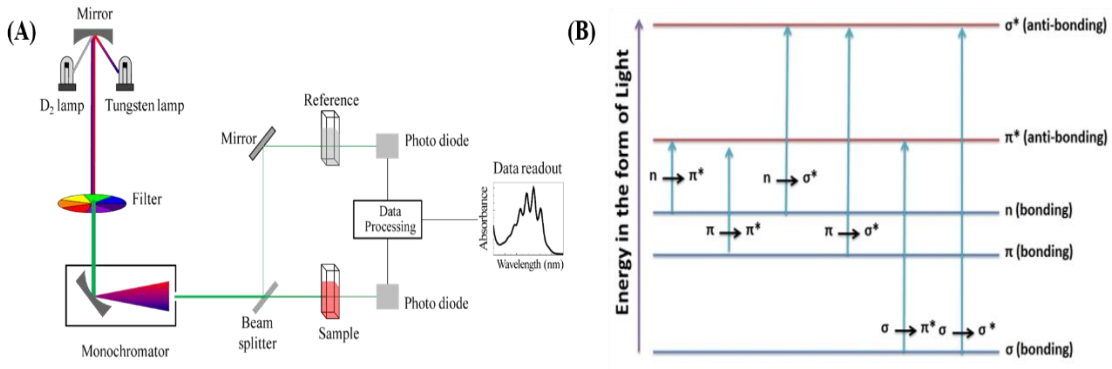

Figure 3. 1 Schematic illustration of **(**A) the operation for UV-Visible spectrometer[1] and (B) various electronic transitions between bonding and anti-bonding state by light absorption[2].

3.2 X-ray Diffractometer (XRD)

X-ray diffraction is a characterization analysis method that measures the crystallographic structure, lattice parameters, planar spacing, and crystallite size of materials. Figure 3.2A shows the schematic illustration of X-ray diffractometer which consist of three basic parts: an X-ray tube, a sample holder, and an X-ray detector. X-rays are generated in cathode ray tube by heating a filament to produce electrons which are collided with target material. The most common X-ray is Cu K_α =1.5418Å which is from single crystal diffraction of Copper target. This X-ray is irradiated and collimated onto the sample. With the sample and detector are rotated, the intensity of refracted X-rays is recorded on the detector.[3] The Bragg's law (eq. 1) is the basic theory of the XRD instrument. Figure 3.2B indicate the Bragg's law. The interaction of incident X-ray (S_0) with the atoms located in the lattice produce the constructive or destructive interference when it satisfies the Bragg's law. This law gives information for the diffraction angle and the lattice spacing in a crystalline sample. The diffracted X-rays (S_1) are detected and counted to the detector. The sample is scanned through a range of 2θ angles, and all of possible diffraction of the lattice are detected due to the random orientation of powdered materials.[4]

$$n\lambda = 2d\sin\theta \quad \cdots\cdots\cdots (1)$$

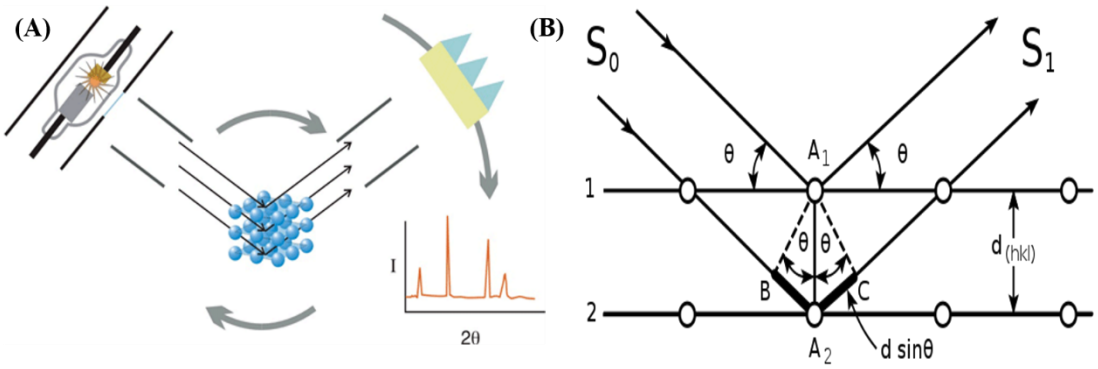

Figure 3. 2 Schematic illustration of (A) X-ray diffractometer operation[3] and (B) Bragg's law[4].

3.3 X-ray Photoelectron spectrometer (XPS)

X-ray photoelectron spectroscopy (XPS) provides a standard experimental tool for the surface analysis. XPS has very high surface sensitivity due to the extremely small mean free paths of electrons with kinetic energies in the range of 10-2000 eV. Photoelectrons are detected in terms of their energy and momentum distribution. The basic process of XPS analysis is illustrated in Figure 3.3A, where photons with specific energy are used to excite the electrons in atom below the surface of the sample. Electrons ejected from the surface are filtered with the kinetic energy by analyzer. The resulting spectra exhibit resonance peaks characteristic of the electronic structure of sample atoms.[5]

In principle, the X-rays having higher energy are entered into electronic states of the atoms and the electrons in core-level are ejected by X-rays. The kinetic energy of ejected electrons is an important indicator to calculate the binding energy of the element. Because the binding energies of the electron in atoms are known, the position of peaks in the spectrum can allow some information such as the atomic composition and quantitative analysis of the surface of samples. Besides, Chemical bonding will frequently have an effect on the binding energy of the electron orbital and give rise to an observable chemical shift in the kinetic energy of the photoelectron. These binding energy shifts can be used to extract information of a chemical nature, such as atomic oxidation state.[6]

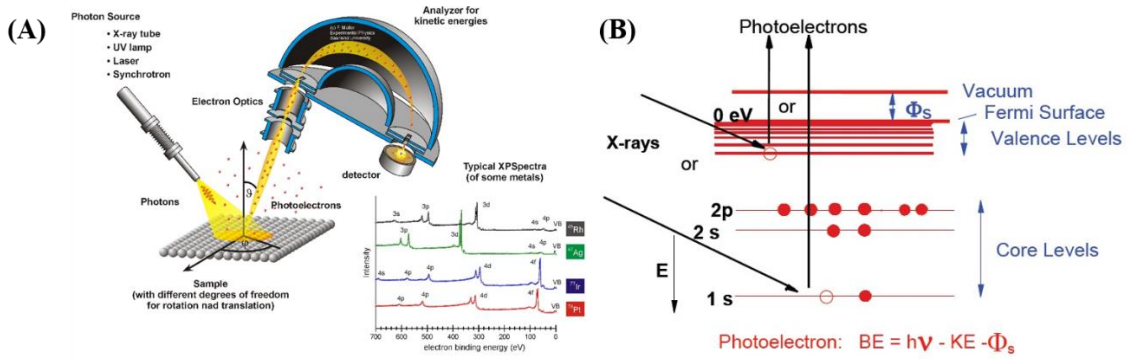

Figure 3. 3 Schematic illustration of (A) the principle of X-ray photoelectron spectrometer[5] and (B) the process of photoelectron generation in electronic structure of the atom[6].

3.4 Transmission Electron Microscope (TEM)

Transmission Electron Microscopy (TEM) is a microscopy technique in which a beam of electrons is transmitted through an ultrathin specimen, interacting with the specimen as it passes through. Figure 3.4A shows a schematic illustration of a TEM. There are four parts in TEM: electron source, Electromagnetic lens system, sample holder, and imaging system.[7] The electron beam is generated in electron source which is consist of cathode and anode. The beam is accelerated toward the specimen by the positive anode. In electromagnetic lens system, the electron beam is tightly focused by electromagnetic lens and metal apertures. After passing through the lens system, the focused electron beam penetrates the specimen and make an image on fluorescence screen. When the electron beam passes through a thin specimen, various scatter electrons are generated. Figure 3.4B shows the various scattered electron modes. The TEM, HRTEM (high-resolution TEM), and ED (electron diffraction) uses elastic scattered electrons for structure or crystallinity analysis. The inelastic scattered electrons are used as EELS (electron energy loss spectroscopy) and EFTEM (energy filtered TEM). These kinds of method can analyze atomic composition and chemical analysis.[8]

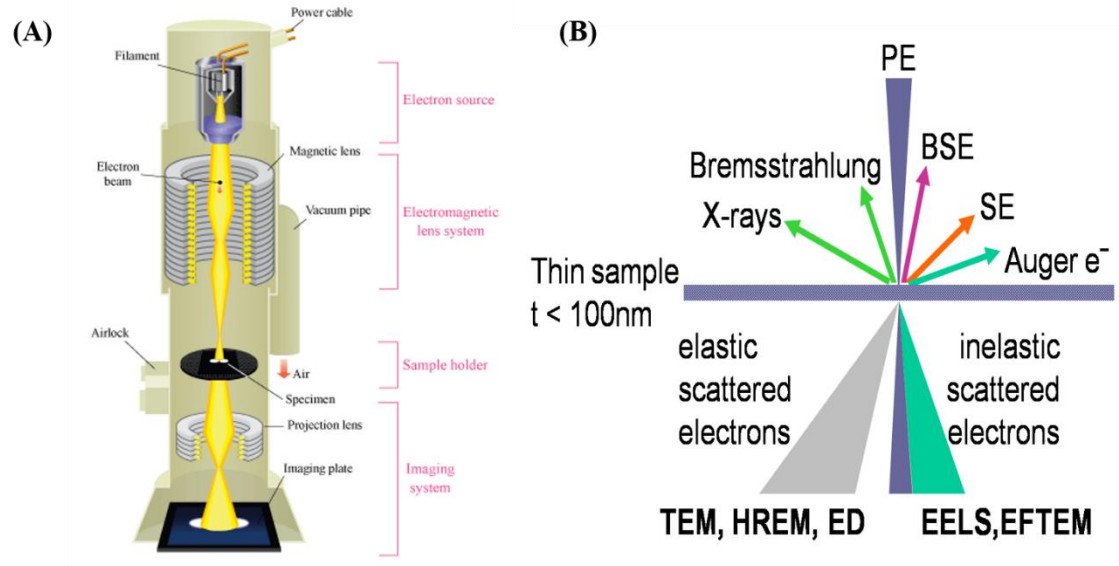

Figure 3. 4 Schematic illustration of (A) TEM[7] and (B) various scattered electron modes when the electron beam is irradiated into the specimen[8].

3.5 Brunauer-Emmett-Teller (BET) Specific Surface Area Analyzer

The specific surface area of a powder is determined by physical adsorption of a gas on the surface of the solid and by calculating the amount of adsorbate gas corresponding to a monomolecular layer on the surface. The determination is usually carried out in the temperature of liquid nitrogen. The amount of gas adsorbed can be measured by a volumetric or continuous flow procedure. Figure 3.5A shows that schematic diagram of the BET operation. In multi-point measurement, the data are treated according to the Brunauer, Emmett and Teller (BET) adsorption isotherm equation[9]:

$$\frac{1}{\left[V_a\left(\frac{P_0}{P}-1\right)\right]}=\frac{C-1}{V_m C}\times\frac{P}{P_0}+\frac{1}{V_m C}$$

P = partial vapor pressure of adsorbate gas in equilibrium with the surface at 77.4 K (b.p. of liquid nitrogen), in Pascal,

P_0= saturated pressure of adsorbate gas, in Pascal,

V_a= A volume of gas adsorbed at standard temperature and pressure (STP) in milliliters,

V_m= A volume of gas adsorbed at STP to produce an apparent monolayer on the sample surface, in milliliters,

C= dimensionless constant that is related to the enthalpy of adsorption of the adsorbate gas on the powder sample.

Figure 3.5B shows the basic principle of BET analysis. There are four steps of gas adsorption: i) adsorption at isolated site, ii) forming monolayer, iii) filling multilayer, and iv) condensation of gas molecules.[10] Many information such as specific surface area, pore volume, pore size, and distribution are extracted from these processes.

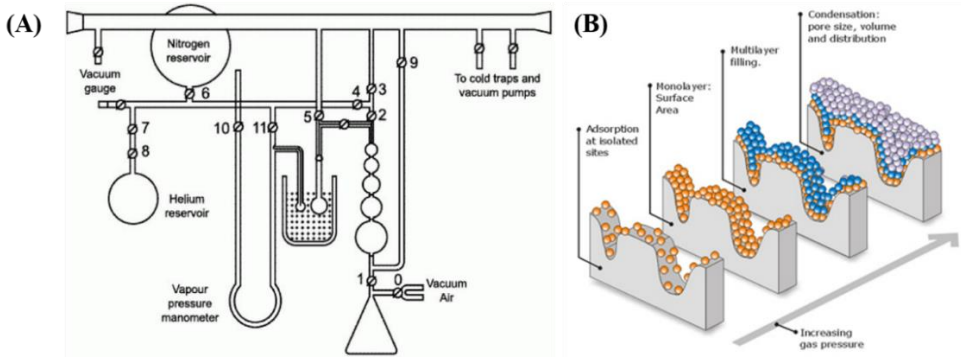

Figure 3. 5 Schematic diagram of (A) dynamic flow method[9], and (B) basic principle of BET[10].

3.6 Gas Chromatography (GC)

Gas chromatography (GC) is a common type of chromatography used in analytic chemistry for separating and analyzing compounds that can be vaporized without decomposition. Figure 3.6A shows that the basic process of GC analysis. A method of analysis is vaporized and introduced into a stream of carrier gas such as He or N_2. It is carried out through a chromatographic column and separated into its constituents. These fractions pass through the column at characteristic rates, and are detected as they emerge in a time sequence. The detecting responses are recorded on a chart, from which the components can be identified both qualitatively and quantitatively.[11]

GC detectors can be classified into two groups, universal and selective detectors based on their general response to specific elements or ions. Flame-ionization detector (FID) is the most commonly used detector in GC. The other detectors include electron-capture detector (ECD), thermal conductivity detector (TCD), nitrogen-phosphorus or thermionic specific detector (NPD or TSD), flame photometric detector (FPD) and mass spectrometric detectors (MSD). For quantitative analyses, detectors must have a wide linear dynamic range: the response must be directly proportional to the amount of compound present in the detector over a wide range of concentrations. FID has a wide linear range (~10^6) and is sensitive to organic compounds. FID with either helium or nitrogen carrier gas are to be used for packed columns, and helium is used for capillary columns. TCD detects changes in the thermal conductivity of the gas stream as solutes are eluted. Although its linear dynamic range is smaller than that of the FID, it is quite rugged and occasionally used with packed columns, especially for compounds that do not respond to FID.[12] In our group, we are using two kinds of detector, FID and TCD to detect short alkyl chain (methane) and carbon dioxide.

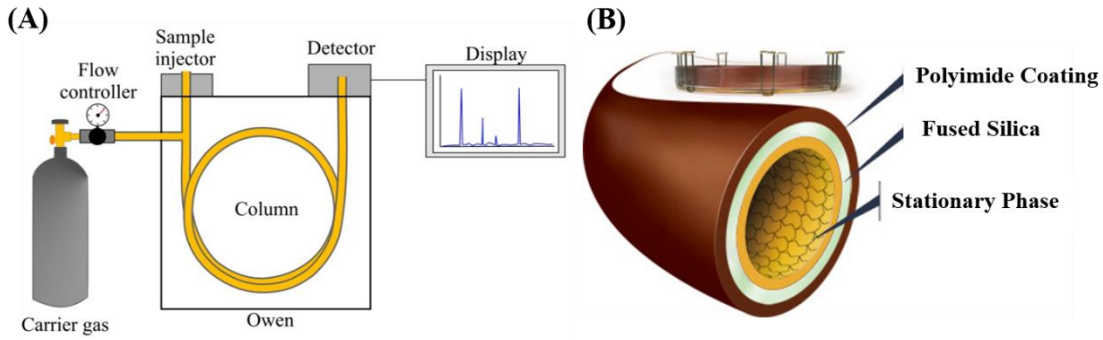

Figure 3. 6 Schematic illustration of (A) the operation of GC[11] and (B) the components of column[12].

There are three basic components in column: i) polyimide coating, ii) fused silica, and iii) stationary phase (Figure 3.6B). In gas-solid chromatography, the stationary phase is an active adsorbent, such as alumina, silica, carbon or a polyaromatic porous resin, packed into a column. The passage of solute through the column will be retarded by adsorption or exclusion mechanisms in Figure 3.7. When a volatile compound is introduced into the carrier gas and carried into the column, it is partitioned between the gas and stationary phases by a dynamic countercurrent distribution process. The compound is carried down the column by the carrier gas, retained to a greater or lesser extent by sorption and desorption in the stationary phase.[13]

The elution of the compound is characterized by the partition ratio, *k*, a dimensionless quantity also called the capacity factor. It is equivalent to the ratio of the time required for the compound to flow through the column (retention time) to that of an unretained compound. The value of the capacity factor depends on the chemical nature of the compound; the nature, amount, and surface area of the liquid phase; and the column temperature. Under a specified set of experimental conditions, a characteristic capacity factor exists for every compound. Separation by gas chromatography occurs only if the compounds concerned have different capacity factors

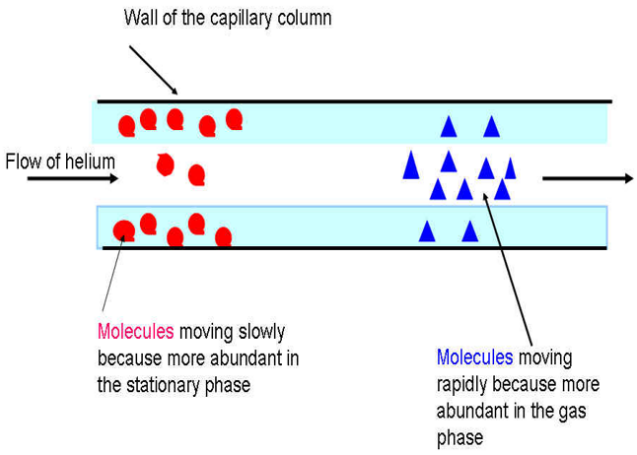

Figure 3. 7 Schematic illustration of the separation of different molecule species in a capillary column.[13]

3.7 References

1. http://en.wikipedia.org/wiki/Ultraviolet%E2%80%93visible_spectroscopy
2. http://pharmaxchange.info/press/2011/12/ultraviolet-visible-uv-vis-spectroscopy-principle
3. http://ees2.geo.rpi.edu/probe/Images/concepts/concept2.html
4. http://commons.wikimedia.org/wiki/File:Bragg_diffraction.svg
5. http://jacobs.physik.uni-saarland.de/instrumentation/uhvl.htm
6. http://subato.blogspot.kr/2011/05/material-surface-analysis-with-x-ray.html
7. http://www.hk-phy.org/atomic_world/tem/tem02_e.html
8. http://portal.tugraz.at/portal/page/portal/felmi/research/TEM%20and%20Nanoanalysis/Principles%20of%20TEM
9. http://particle.dk/methods-analytical-laboratory/surface-area-bet/surface-area-bet-theory
10. http://www.particletesting.com/Services-Provided/Surface-Area.aspx
11. http://elte.prompt.hu/sites/default/files/tananyagok/atmospheric/ch15s02.html
12. http://www.thetruthaboutforensicscience.com/the-top-2-problems-seen-with-gas-chromatography-bac-results
13. http://www.specmetcrime.com/introduction_%C3%A0_la_gcms.htm

4. Photocatalytic Conversion of CO_2 gas to Hydrocarbon Fuel using Carbon and Nitrogen co-doped Sodium Titanate Nanotubes.

4.1 Introduction

The excessive release of CO_2 into atmosphere is considered as a major cause for the challenging issues of global warming, climate changes and environmental pollution. To overcome the issue of increased atmospheric CO_2 concentration, one effective approach is to convert atmospheric CO_2 to hydrocarbon fuels. In this regard, numerous titanium (Ti) based photocatalysts[1,2,3] have been developed and investigated for photocatalytic conversion of CO_2 into hydrocarbons. Among the photocatalysts, titania (TiO_2) is intensively studied in the respective field. However, due to large band gap, TiO_2 absorbs mainly Ultraviolet (UV) light consisting of only 4-5% of the solar irradiation reaching earth surface[4] thus limiting its application. Therefore, studies have made great attempts to extend the absorption of TiO_2 to visible light range. There are several methods to improve the visible light sensitivity of TiO_2 such as transition metal ion implanted TiO_2[5], reduced TiO_x photocatalysts[6], non-metal doped-TiO_2[7], low band gap energy hybrid nanomaterials[8], dye sensitized TiO_2[9] and TiO_2 doped with up conversion luminescence agent[10]. Furthermore TiO_2 can also form various layered nanostructures such as nanofibers[11], nanosheets[12], nanotubes[13] in which above mentioned modifications are possible with stable nanostructure .

The layered titanate nanotubes or nanosheets have been widely studied because of their attractive properties and extensive range of application.[14] Various advantages possessed by layered titanates include large surface area, appropriate band gap, moderate adsorption capacity, enhanced photocatalytic activity, improved thermal and chemical stability.[15] Despite the wide variety of compositions and crystal structures, layered titanates usually possess moderate characteristics of TiO_2.[16] Although titanate nanotubes have not been investigated as extensively as anatase TiO_2, but they have been demonstrated to possess great potential in many areas of semiconductor nanostructure applications.

Doping of anatase TiO_2 with various nonmetal ions are explored well.[17] However, the simultaneous doping of more than one anions in TiO_2 nanostructure is not explored well. Moreover, the reported literature mentioned only about the co-doped TiO_2 nanoparticles.[18] Carbon and nitrogen have the ability to improve the photocatalytic activity of TiO_2.[19] Therefore, it is necessary to find a facile way to prepare carbon and

nitrogen co-doped TiO_2 nanostructures for improving the photocatalytic activity.

In this study, a carbon and nitrogen co-doped sodium titanate nanotubes (C, N-TNT) were prepared by a simple two step synthesis route involving hydrothermal method followed by calcination treatment. In the first step, the alkaline hydrothermal treatment of available TiO_2 (anatase) produces sodium titanate nanotubes which were then mixed with desired amount of urea and calcined in the second step to achieve C, N-TNT. It is reported, the most stable nanotube structure is obtained via alkaline hydrothermal treatment of TiO_2 (anatase) with NaOH as compared to nanotubes formed when other alkali metal oxides are used.[20] The stable nanotube structure is an important parameter for photocatalytic activity[21], thus herein NaOH was used during alkaline hydrothermal treatment step. A series of the C, N-TNT was prepared by varying the composition of urea and its influence on physico-chemical properties and photocatalytic activity of the materials was demonstrated. The materials were characterized by various instrumental techniques. The photocatalytic activities of C, N-TNT were evaluated towards both, by CO_2 photoreduction to hydrocarbons and methylene blue (MB) dye degradation tests under simulated solar light irradiation. To the best of our knowledge, this is the first report demonstrating the photocatalytic performance of C, N-TNT by photocatalytic conversion of CO_2 into hydrocarbons and MB dye degradation.

4.2 Experimental Section

4.2.1 Materials

Sodium hydroxide (Duksan, 94%), TiO_2 anatase (Duksan, 99.95%), Urea (Sigma aldrich, 98%), Methylene blue (Sigma aldrich) were used without further purification. The deionized water (resistivity > 18μm) was used throughout the experiments.

4.2.2 Methods

Preparation of sodium titanate nanotubes (TNT) The synthesis route followed for preparation of sodium titanate nanotubes is reported earlier.[22] Typically, 2.0 g of commercially available TiO_2 powder (anatase) was mixed with 20 mL of 10 M NaOH solution in a beaker. The suspension was stirred for 1h to get a uniform mixture. The mixture was transferred to a Teflon lined autoclave and heated at 150° C

for 24 hours. The reaction mixture was filtered after cooling and washed with deionized water to adjust the pH to 7. The precipitate obtained was dried at 70 ±10 °C in an air oven, and calcined at 400 °C in a muffle furnace for 6 hours in the presence of static air. This sample was labeled as TNT.

Preparation of carbon and nitrogen co-doped sodium titanate nanotubes (C, N-TNT) In order to prepare a series of carbon and nitrogen co-doped sodium titanate (C, N-TNT), TNT was mixed with varied amount of urea in a mortar and ground well to obtain a homogeneous mixture. Typically 0.1 g of TNT was mixed with 0.1, 0.3, 0.6, and 1.0 g of urea and the obtained powdered samples after grinding were transferred to a crucible and calcined at 400 °C for 3 hours in a tubular furnace under air flow (15 cm^3/min). The obtained materials were labeled as C,N-TNT01, C,N-TNT03, C,N-TNT06, and C,N-TNT1 for the sample obtained with 0.1, 0.3, 0.6, and 1.0 g of urea respectively.

Photocatalytic degradation of methylene blue (MB) The photocatalytic degradation of methylene blue (MB) were performed in a glass beaker containing 10 mg of catalysts and 100 ml of methylene blue (12 mg/L) solution. A 100 W Xenon lamp (Oriel, LCS-100) was used as a solar light source in 1 sun condition. The solution was stirred in dark for 90 min to achieve the steady states of adsorption-desorption equilibrium on the C, N-TNT surface. It irradiates outside 15 cm a distant from the solution surface. After irradiating, the sample was centrifuged to remove all catalysts. The absorption of MB solution was measured at 664 nm using UV-Vis absorption spectroscope. (Agilent Technology, Cary 5000)

Photocatalytic CO_2 Reduction Test The photocatalytic CO_2 conversion experiment with H_2O for various catalysts were performed as reported earlier. Prior to the experiments the photoreactor was purged with vacuum. Before the photocatalyst loading, the reactor was purged with CO_2 gas for 3 times in order to remove any air or other impurities present in the system. 1,000 ppm of high purity CO_2 gas was passed through a water bubbler to allow a mixture of CO_2 and H_2O vapor. A 100W Xenon solar simulator (Oriel, LCS-100) with an AM1.5 filter was used as a light source. For each test, 100 mg of samples were reacted for 1 h and analyzed by gas chromatograph (Shimadzu GC-2014, Restek Rt-Q-Bond column, ID=0.53 mm, length=30 m) equipped with both a thermal conductivity detector (TCD) and a flame ionization detector (FID).

4.2.3 Analysis

Characterization of Catalysts In order to know about the crystalline structure of the materials the samples were analyzed by powder X-ray diffractometry (XRD). The phase transformation of the materials and the band assigned for titanate was studied by Raman spectroscopy. The N_2 physisorption measurement was carried out to know about the textural properties such as specific surface area, pore volume, and pore size distribution. The transmission electron microscopy (TEM) was carried out to know about the morphology and particle size of the materials. The diffuse reflectance UV/Visible spectroscopy (DRS) was measured to calculate the band gap energy of the mixed oxide materials. The surface composition, oxidation states of Ti, O, C and N in different C, N-TNT materials were determined by X-ray photoelectron spectroscopy (XPS).

Powder XRD patterns of the materials were analyzed by using X-ray diffractometer (Pan Analytical, Empyrean) operating at 40 kV and 30 mA with Cu Kα radiation (λ=1.54Å) as an X-ray source and scanned with a rate of 1°/min in the range of 2θ =5-80°. Raman spectra were measured by a NICOLET ALMECA XR Raman spectrometer with a He-Ne laser (532 nm) as the light source. For N_2 physisorption measurements, the samples were degassed extensively at 200 ºC prior to the experiments. The N_2 sorption isotherms were measured at −196 ºC on a Micrometrics ASAP 2000 apparatus. The surface area was calculated by using the Brunauer–Emmett-Teller (BET) equation. The pore volume was determined from the amount of N_2 adsorbed at the highest relative pressure of (P/P_0) =0.99. The BJH pore diameter was obtained by applying the Barrett-Joyner-Halenda (BJH) equation to the desorption isotherm. The TEM image of the bare TNT and C, N-TNT were obtained by FE-TEM (Hitachi HF-3300) instrument operating at 300 kV. Prior to TEM analysis, the samples were dispersed in ethanol followed by sonicating the mixture for 1 hour. One drop of the dilute suspension was placed on a TEM grid and allowed to dry overnight. The DRS were recorded on a Cary series UV-Visible near IR spectrophotometer with a diffuse reflection accessory. The X-ray photoelectron spectroscopy (XPS) analysis was performed on an ESCALAB 250Xi (Thermo Scientific) with Al Kα radiation as the X-ray source.

4.3 Results & Discussion

A synthetic strategy to enhance photocatalytic activity of titanate under visible light irradiation is to intercalate sodium ion (Na^+) and co-dope carbon and nitrogen in lattice of titanate nanotube by hydrothermal and calcination method. The XRD pattern of bare TNT and C, N-TNT samples are shown in Figure 4.1. The samples exhibit diffraction peaks at 2θ values of 10.2º, 24.2º, 28.6º, 33.8º, 38.6 ºand 61.6º corresponding to d_{200}, d_{110}, d_{310}, $d_{31\text{-}2}$, d_{004} and d_{020} respectively, indicating the presence of titanate phase.[23] The peak at 10.2 º is slightly redSh shifted and show lower intensity of peaks in C, N-TNT compared to bare TNT. It is known that TNT proceed with a local shrinkage and phase transformation when calcined in air. In particular, the exchange of Na^+ ions by H^+ ions would significantly promote the destruction process.[24] The dissociated H^+ ions from urea may attack the Ti-O bonds of TNT, leading to the destruction of nanotube walls. Figure 4.2 shows the TEM image of bare TNT and C, N co-doped TNT. The image in Figure 4.2A reveals that the bare TNT has tubular structure with a crystalline multiwall and 10~12 nm of diameter. Figure 4.2B demonstrates that the C, N-TNT06 retain tubular structure after C, N co-doping at 400 ℃. However, the nanotubes are slightly destroyed due to grinding and calcination process to co-dope C and N in TNT.

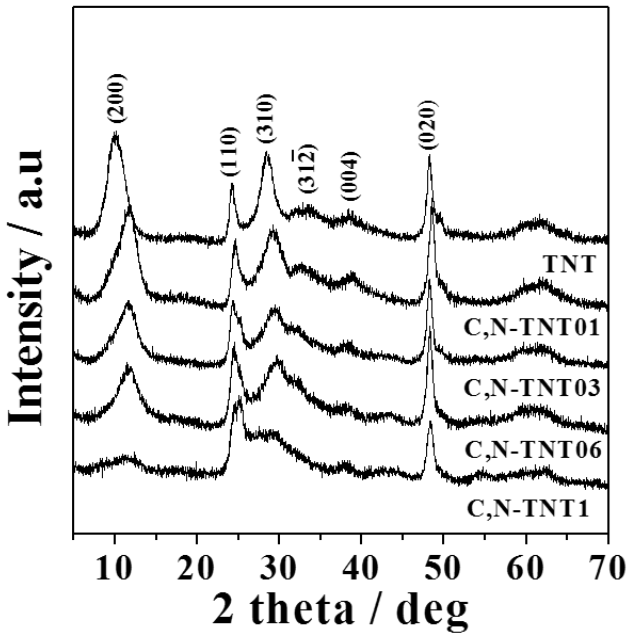

Figure 4. 1 XRD patterns of the bare TNT and a series of C, N-TNT

STEM images of the bare TNT and the representative of the C, N-TNT were shown in Figure 4.3. The morphology of bare TNT and the representative of the C,N-TNT, C,N-TNT06 are tubular in shape. There are many island having porous structure by significant aggregation for the bare TNT and C,N-TNT. (Figure 4.3 A and C) However, the scale of island was reduced and some of the nanotubes were slightly distorted by attacking of H^+ from urea during calcination process. It may related with the enhancement of surface area for C,N-TNT.

The light absorption and its bandgap energy were determined by Uv-vis Diffuse Reflectance Spectroscopy (Uv-vis DRS) and tauc translation plot. UV-vis DRS of bare TNT and C, N-TNT were shown in Figure 4.4A. The light absorption below 400 nm is attributed to the electron transitions from the valence band to the conduction band. A red shift was observed in absorption wavelength when the amount of urea is increased[4], inferring to changes in the doping level of carbon and nitrogen in TNT. It is evident that C, N-TNT samples show large optical absorbance in the visible region extended from 400 nm to 500 nm as the amount of urea increases. This can be associated to the synergistic effect of C and N codoping, resulting in the shift of light absorption to the visible region and narrowing down the bandgap. Band gaps of all the samples were estimated using Tauc plot (Figure. 4.4B).

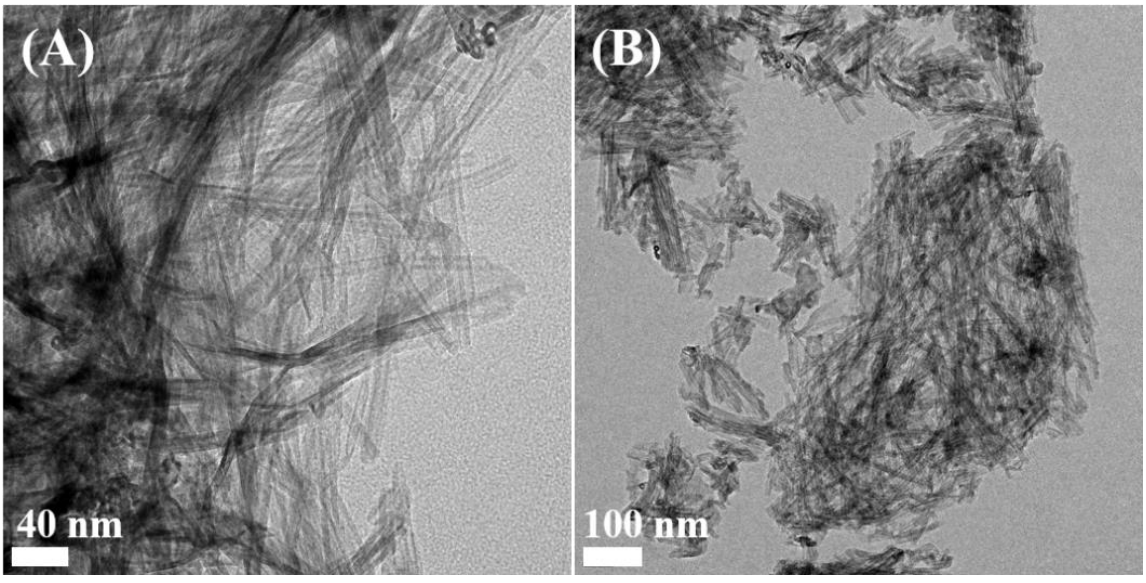

Figure 4. 2 TEM images of (A) the bare TNT and (B) C,N co-doped TNT

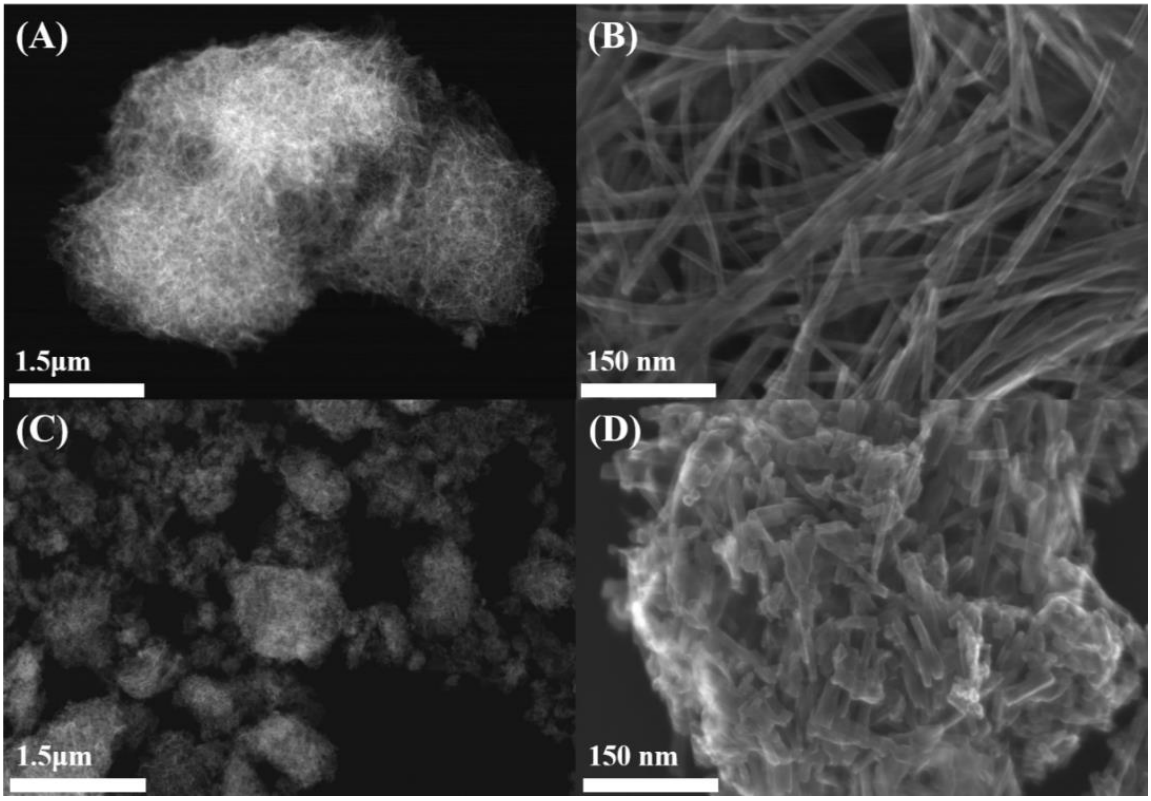

Figure 4. 3 STEM images of (A and B) the bare TNT and (C and D) C,N co-doped TNT

The band gaps estimated for each material were shown in Table 4.1. It is obvious that all the C,N-TNT samples show lower band gap as compared to the bare TNT. The variation in band gap was attributed to the difference in loading amount of carbon and nitrogen dopant in these materials. The Raman spectroscopy was introduced to identify the intercalation of Na^+ between the multiwall and co-doping of C and N by vibration mode. The Raman spectra of TNT and C, N-TNT were shown in Figure 4.5. All of the materials displayed broad Raman active bands at 280, 445, 675, and 908 cm^{-1} respectively. The band at 285 cm^{-1}, and 675 cm^{-1} corresponds to Ti-O-Na stretching vibration of TNT as reported earlier by Qamar *et al.*[25] The bands at 445 and 675 cm^{-1} of TNT are due to Ti-O-Ti. The vibrational band at 908 cm^{-1} result from the stretching vibration of Ti-O involving non-bridging oxygen atom coordinated with sodium ions. Even though the intensity of band at 908 cm^{-1} reduced after the addition of urea to TNT, still the band at 908 cm^{-1} is present in all of the materials indicating that partial exchange of sodium ions present in TNT with hydrogen ion. The materials C, N-TNT03, C, N-TNT06, and C, N-TNT1 show bands at 141 cm^{-1} and 198 cm^{-1} are due to a small amount of anatase TiO_2 in these materials.[26]

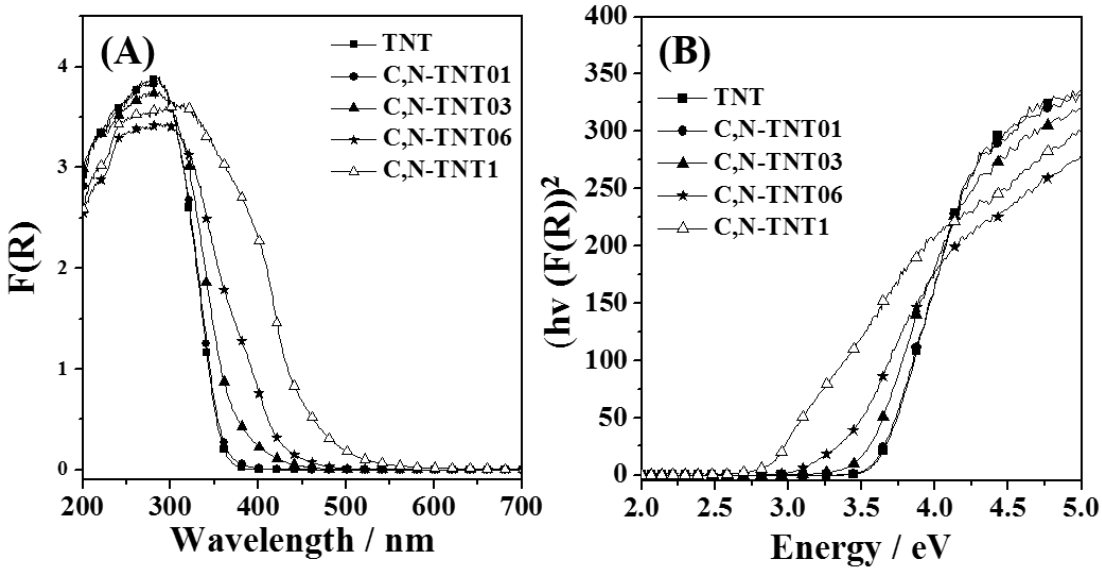

Figure 4. 4 UV-Vis diffuse reflectance spectra of the C, N-TNT (A). Corresponding Tauc plot (B). The bare TNT is also shown for comparison.

Figure 4.6 shows the N_2-sorption isotherms of the TNT and C, N-TNT samples, respectively. The N_2-sorption results reveal that the isotherms of TNT and C,N–TNT samples are of type IV according to the IUPAC classification.[27] They initially exhibit a monolayer adsorption at low relative pressures, followed by a steep rise that represents multilayer adsorption and this is eventually followed by capillary condensation that occurs in the mesopores at high relative pressure. Due to the differences in pressures at which capillary evaporation and condensation take place, the isotherms display H3 hysteresis loops revealing the existence of aggregated plate-like particles with slit-like pores.[27] The BET specific surface area of the C,N-TNT samples are fairly close to the surface area of bare TNT. The samples C,N-TNT01, C,N-TNT03, C,N-TNT06 shows almost equal surface area and similar pore size distribution as that of bare TNT, which indicate that the C,N- codoping do not make much variation in the textural properties of these material. The material C,N-TNT1 show slightly lower surface area and pore volume compared to bare TNT indicating that C,N doping making slight variation in this material. The pore volume of C, N-TNT1 is 0.32 nm, while TNT shows slightly higher pore volume (0.42 nm).

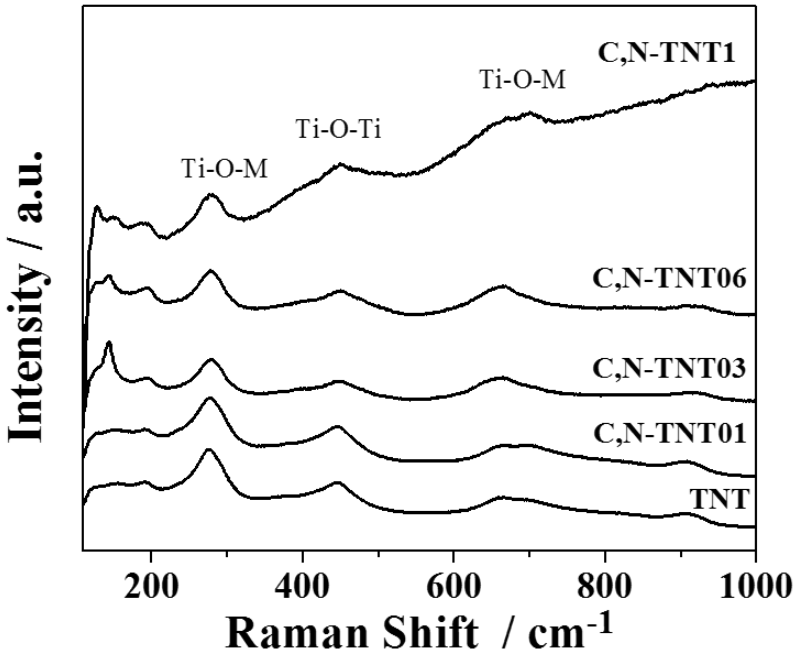

Figure 4. 5 Raman spectra of the bare TNT and C, N-TNT

The BJH pore size distributions of TNT demonstrate relatively wide spread mesoporosity and macroporosity ranging from 5 to 70 nm with the majority of pores centered around 16 nm as shown in the Figure 4.6B. The macroporosity seem to arise from the pores formed between various TNT particles, i.e. intra-particle pores. The BJH pore size distributions of C, N-TNT01, C, N-TNT03, C, N-TNT06, C, N-TNT1 indicates the presence of relatively similar mesoporosity and same macroporosity as that of TNT. The textural properties, including specific surface area, pore volume, and average pore diameters obtained from nitrogen adsorption-desorption analysis, were shown in Table 4.1. The survey scan XPS spectra of bare TNT and C, N-TNT samples are shown in Figure 4.7A which, clearly indicate that Ti, O, N, and C elements exist in the C, N-TNTs, no trace of unwanted impurities are observed in these materials. The high-resolution XPS spectra of the N 1s is shown in Figure 4.7B. The atomic % of elements are also shown in Table 4.2. The TNT and lowest urea treated sample C, N-TNT01 do not show any peak corresponding to N 1s. Similar from the atomic % the amount of C, Ti, and O present in these samples are almost same indicating that small amount of urea treatment does not make any significant variation in the TNT composition. Moreover, the peak corresponding to N 1s in these material, indicates the absence of nitrogen doping.

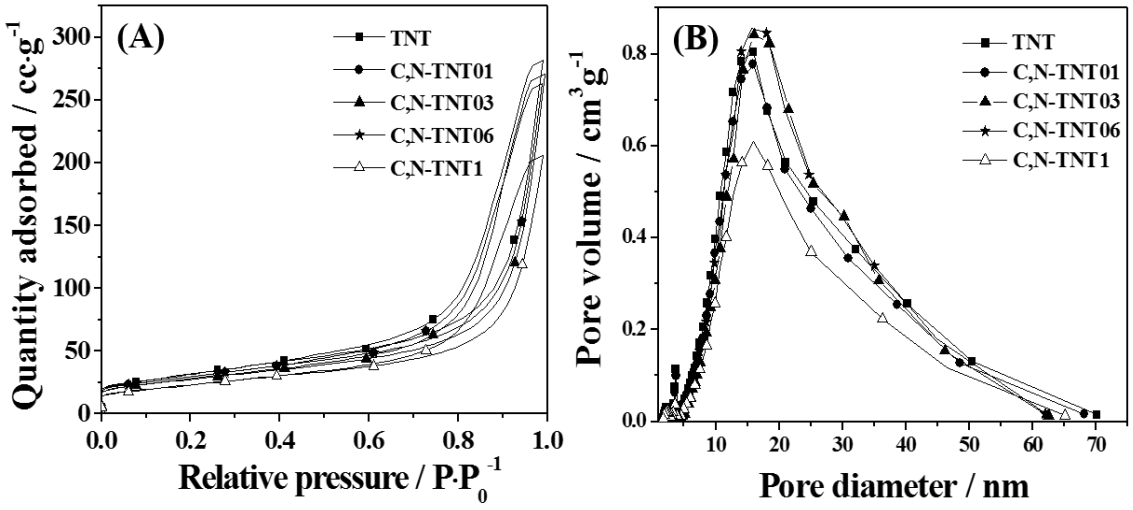

Figure 4. 6 Nitrogen physisorption isotherms (A) and pore size distribution (B) of bare TNT and C, N-TNT samples. (01, 03, 06 and 1 stands for 0.1, 0.3, 0.6, and 1.0 g of urea respectively for C, N-TNT)

The N 1s spectra of C, N-TNT03 and C, N-TNT06 can be best fitted as a combination of two peaks at 399.2 eV and 397.0 eV. The peak at 399.2 eV can be assigned to N atoms from chemisorbed N-containing compounds[28], while the N 1s at 397.0 eV can be attributed to N atoms that replace O atoms in TNT and form Ti-N bonds.[29] The amount of N doped in C,N-TNT06 was higher than C,N-TNT03. The highest amount of urea treated TNT material, C, N-TNT1 show band at 396 eV in the XPS spectra which is attributed to a chemically bound N-species[30] within the crystalline TiO_2 lattice and 394.7 eV due to atomic nitrogen formed by dissociation of a small fraction of the adsorbing molecules.[31] The amount of N doped in C, N-TNT1 is found to be highest among the series. XPS spectrum of C 1s is shown in Figure 4.7C, the strong single peak located at 284.6 eV is ascribed to the elemental carbon.[32] The peaks with binding energies at 286.1 and 288.3 eV are attributed to C–O and C=O bonds, respectively, which indicates the formation of carbonated species and a probable substitution of lattice titanium ions to form Ti–O–C bonding.[32] Furthermore, the absence of Ti–C bond around 281 eV suggests the carbon atoms do not enter into the TNT lattice. The high resolution XPS spectrum of Ti 2p regions is shown in Figure 4.7D. Two intense peaks at 458.7 eV and 464.5 eV are observed for TNT and C, N-TNT, corresponding to the Ti $2p_{3/2}$ and Ti $2p_{1/2}$ binding energy region, which indicates the presence of Ti^{4+} ions in TNT. Furthermore, Figure 4.7E displays spectra corresponding to O 1s region for both of these materials. They reveal the presence of three peaks corresponding to Ti-O bond (530.0 eV), O-H bond (531.4 eV), and C-O bond (532.5 eV) respectively.

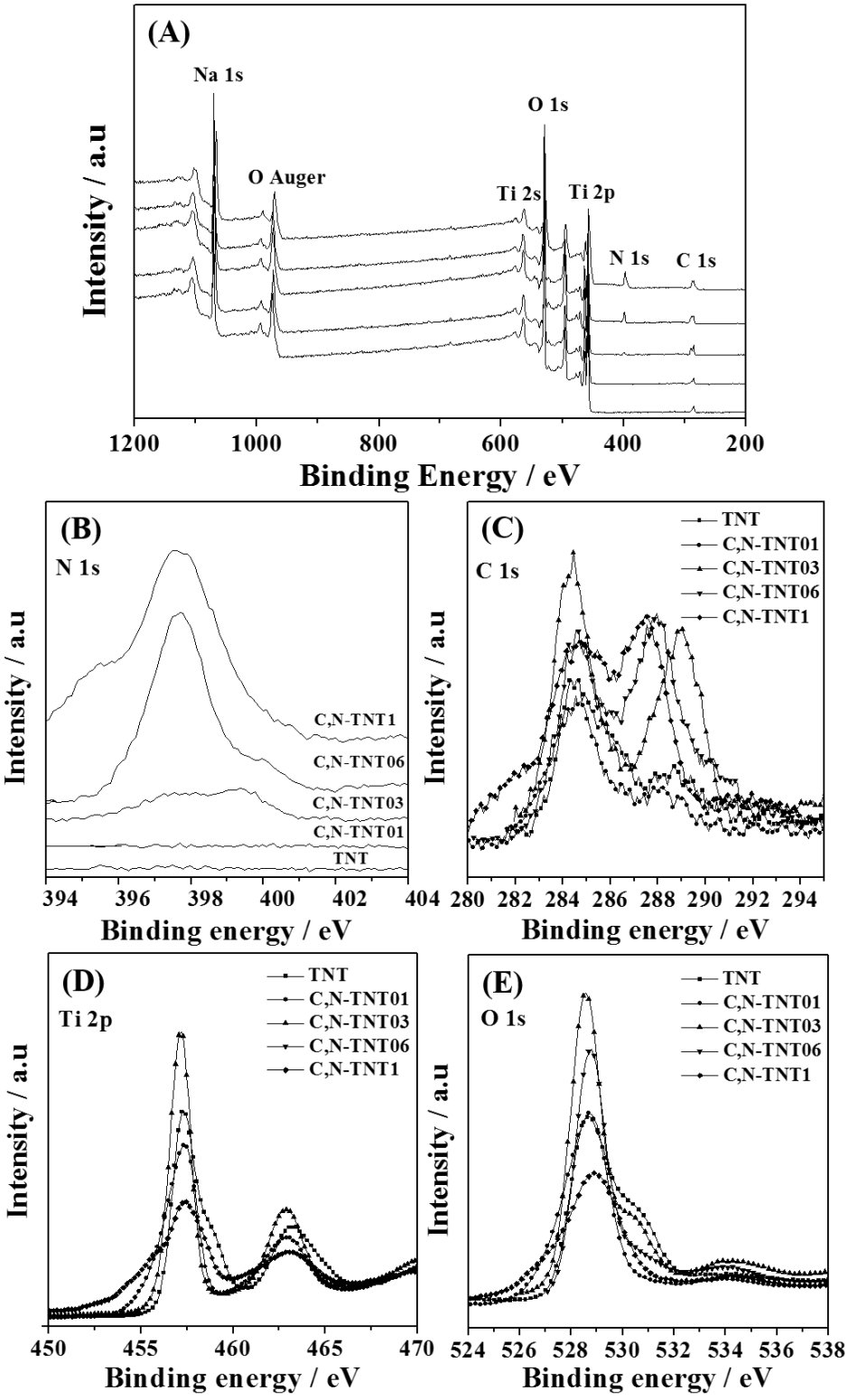

Figure 4. 7 X-ray Photoelectron spectra of (A) survey, (B) N 1s, (C) C 1s, (D) Ti 2p, and (E) O 1s, for bare TNT and C, N-TNT

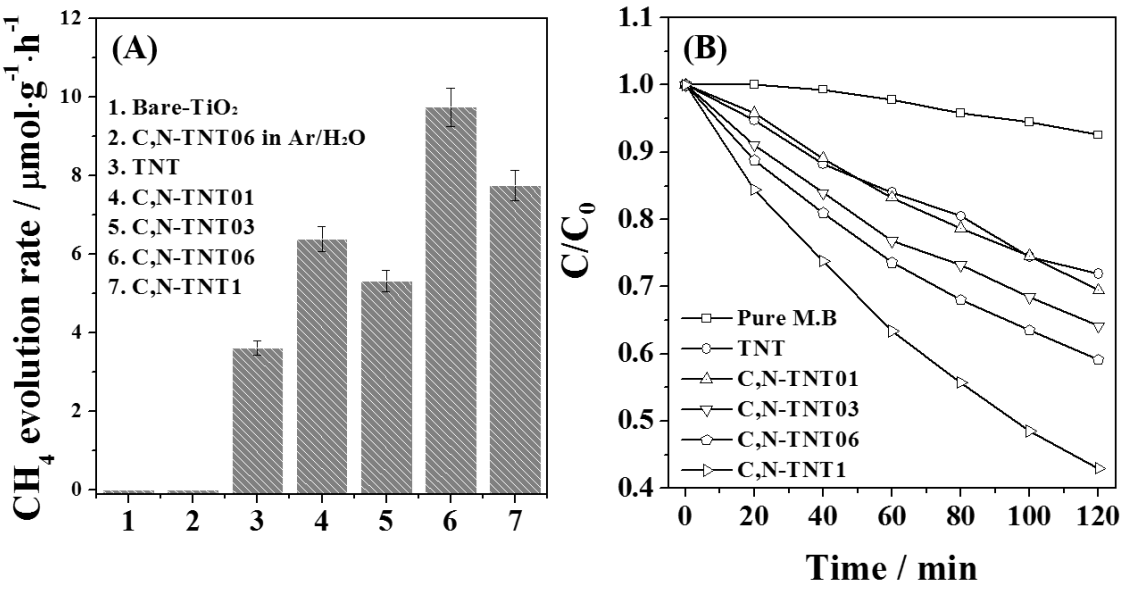

Figure 4. 8 (A) photocatalytic conversion of CO_2 into CH_4 and (B) Degradation of Methylene blue (after 1 h irradiation) by C, N co-doped TNT under simulated solar light irradiation

Photocatalytic activity of bare-TNT and C, N-TNT samples were demonstrated by photocatalytic conversion of CO_2 into CH_4 and MB dye degradation tests under simulated solar light irradiation. The photocatalytic conversion of CO_2 was carried out in gas phase with water vapors. The photocatalytic activity of the prepared materials were evaluated by the amount of methane (CH_4) produced during the photoreduction of CO_2. The CH_4 evolution from CO_2 photoreduction for a series of C, N-TNT samples is shown in Figure 4.8A. During the photocatalytic CO_2 reduction reaction, CO_2 was reduced to CH_4 in presence of H_2O vapors under simulated solar irradiation. The amount of dopants has a significant influence on the photocatalytic CO_2 reduction of TNT. It is obvious from Figure 4.8A, the activity of C, N-TNT01 was enhanced by a small amount of co-doped C, N species. Whereas, in case of C, N-TNT03, the photocatalytic CH_4 evolution was decreased comparatively to C, N-TNT01 sample. The possible reason for decreased photocatalytic activity may be the lower BET specific surface area of C, N-TNT03 as compared to C, N-TNT01 (Table 4.1). The sample C, N-TNT06 shows the highest CH_4 evolution (9.75 μmol/g, 1 h irradiation), which is about 2.7 times higher than that of bare TNT (3.7 μmol/g, 1 h irradiation). When the amount of dopants is further increased than C, N-TNT06, the photocatalytic CH_4 evolution is decreased and can be attributed to the low BET specific surface area (Table 4.1).

The photocatalytic mechanism for CH_4 formation employing C, N-TNT samples is proposed and illustrated in scheme 4.1. It is known that C and N codoping of TNT induces C 2p and N 2p isolated states above the valence band maximum.[19] These isolated states may be responsible for shifting the light absorption of C, N-TNT samples to visible range thus allowing the sub band gap excitations. Upon illumination, pairs of electron (e^-) and hole (h^+) are created at the active sites in TNT and C, N-TNT samples. The holes (h^+) will react with adsorbed H_2O, producing O_2 and H^+ ions. Whereas the CO_2 adsorbed on the materials surface will interact with the electrons (e^-) and H^+ ions, converting to CH_4. It can be assumed here the combination of BET specific surface area and band gap induces optimum conditions for photocatalytic CO_2 conversion into methane.

The photocatalytic activities of the prepared C, N codoped sodium titanate nanotubes were further investigated by photodegradation of MB dye. An improvement in the photodegradation of MB dye is observed when C and N sodium titanate nanotubes are employed. Figure 4.9 shows the comparison of degradation rate curves for various photocatalysts under simulated solar light irradiation for 2 hours. C_0 represents the initial concentration after achieving adsorption-desorption equilibrium and C represents the actual concentration of MB dye at the respective irradiation time. It can be seen that the pure MB shows a very weak degradation under irradiation.

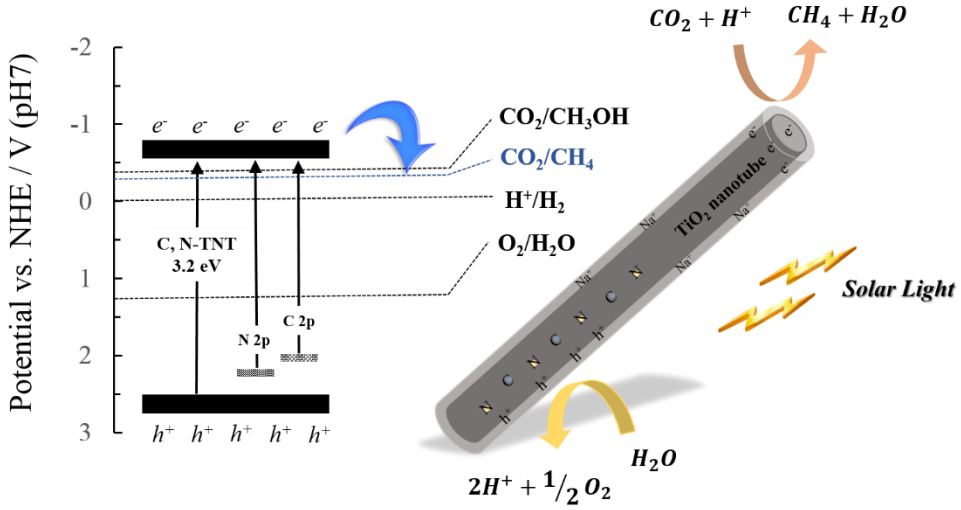

Scheme 4. 1 Schematic illustration for photocatalytic CH_4 evolution reaction of C, N-TNT.

However, when C, N-TNT are employed, the degradation rate of MB increases continuously with the increase of dopants amount. The highest degradation rate was observed with C, N-TNT1, at the mass ratio of Urea:TNT=10:1. About 58% of MB is decomposed by the C, N-TNT1 after 2 hours of irradiation. In contrast, less than 30% of MB decompose after same time of irradiation for bare-TNT and C, N-TNT01. In order to evaluate the catalytic efficiencies of the prepared samples, the rate constants (k) for the photocatalytic reactions of MB degradation were calculated using an equation $\ln (C_0/C) = kT$ based on first order kinetics[33] (Figure 4.9A). Since photocatalytic degradation follows first-order kinetics thus the slope of linear regression represents the apparent reaction rate constant k. It is obvious from Figure 4.9B, the C, N-TNT1 sample exhibits the highest rate constant of 0.00701 min^{-1} for MB dye degradation. This rate constant is 2.5 times higher as compared to bare-TNT. It is reasonable here to consider the suppression of electron-hole recombination in the MB dye as a key factor for enhanced dye degradation. As mentioned earlier, C and N codoping in the TNT system creates isolated C 2p or N 2p states above the valence band maximum of TNT shifting the optical absorption to visible range. The absorption improvement of as prepared materials leads to increased photoexcited electrons resulting in the enhanced degradation of MB dye.[19]

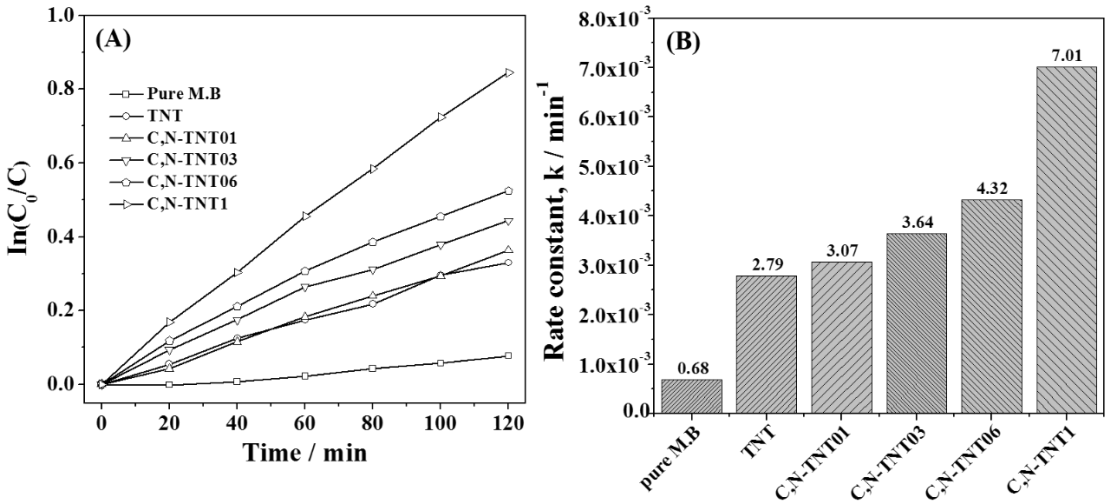

Figure 4. 9 Dye degradation curves (A) and Rate constant versus catalysts diagram (B) employing pure MB, TNT and C, N co-doped TNT samples.

Table 4. 1 Textural properties and photocatalytic CH_4 evolution rate for TNT and C,N-TNT samples

Materials	S_{BET} ($m^2 \cdot g^{-1}$)[a]	Pore volume ($cm^3 \cdot g^{-1}$)[b]	Band gap energy (eV)[c]	Amount of CH_4 ($\mu mol \cdot g^{-1} \cdot h^{-1}$)
TNT	114	0.44	3.46	3.61
C,N-TNT01	105	0.40	3.44	6.39
C,N-TNT03	98	0.42	3.3	5.32
C,N-TNT06	100	0.43	2.8	9.75
C,N-TNT1	83	0.32	2.4	7.75

[a] Surface area determined by applying Brunauer-Emmett-Teller (BET) equation to a relative pressure (P/P_0) range of 0.05-0.35 of the adsorption isotherm.

[b] Pore diameter is calculated from the Barrett-Joyner-Halenda (BJH) equation using the desorption isotherm.

[c] Band gap energies estimated from Tauc plots.

Table 4. 2 C, N, Na, Ti and O atomic composition for TNT and a series of C,N-TNT samples

Material	C 1s (Atomic %)	N 1s (Atomic %)	Ti 2p (Atomic %)	O 1s (Atomic %)
TNT	7.59	--	20.12	52.47
C,N-TNT01	7.97	--	20.14	52.89
C,N-TNT03	11.15	1.37	16.52	49.93
C,N-TNT06	14.59	5.8	15.56	43.86
C,N-TNT1	15.59	11.95	14.5	40.33

4.4 Conclusions

In summary, bare TNT and C, N co-doped TNT were prepared by hydrothermal method followed by calcination process. The photocatalytic performance of the prepared samples were investigated for photocatalytic conversion of CO_2 into CH_4 and MB dye degradation. The prepared materials were characterized by various analytical instruments such as XRD, TEM, SEM, Raman, XPS, and BET. A red shift in absorption wavelength of C, N co-doped TNT samples is observed when the amount of urea is increased. The absorption enhancement is due to the isolated N and C 2p states above the valence band maximum of the TNT. From photocatalytic conversion of CO_2 it is clear that all the C, N co-doped TNT samples exhibits higher CH_4 evolution rate as compared to bare TNT. The improvement in the CH_4 evolution is attributed to the increased BET specific surface area and broadened light absorption. The lower BET specific surface areas of C, N co-doped TNT03 and C, N co-doped TNT1 samples is expected to decrease the photocatalytic conversion of CO_2 when the respective samples are employed. The photocatalytic degradation of MB dye shows a continuous improvement in photocatalytic activity of C, N co-doped TNT samples with increase in the amount of dopants. The photocatalytic activity improvement for dye degradation might be due to broadened absorption and effective prevention of electron hole recombination.

4.5 References

1. Tahir, M.; Amin, N. S., Advances in visible light responsive titanium oxide-based photocatalysts for CO_2 conversion to hydrocarbon fuels. *Energy Conversion and Management* **2013,** *76* (0), 194-214.
2. Liu, G.; Hoivik, N.; Wang, K.; Jakobsen, H., Engineering TiO_2 nanomaterials for CO_2 conversion/solar fuels. *Solar Energy Materials and Solar Cells* **2012,** *105* (0), 53-68.
3. Anpo, M., Photocatalytic reduction of CO_2 with H_2O on highly dispersed Ti-oxide catalysts as a model of artificial photosynthesis. *Journal of CO_2 Utilization* **2013,** *1* (0), 8-17.
4. Dalrymple, O. K.; Stefanakos, E.; Trotz, M. A.; Goswami, D. Y., A review of the mechanisms and modeling of photocatalytic disinfection. *Applied Catalysis B: Environmental* **2010,** *98* (1–2), 27-38.
5. Fuerte, A.; Hernandez-Alonso, M. D.; Maira, A. J.; Martinez-Arias, A.; Fernandez-Garcia, M.; Conesa, J. C.; Soria, J., Visible light-activated nanosized doped-TiO_2 photocatalysts. *Chemical Communications* **2001,** (24), 2718-2719.
6. Ihara, T.; Miyoshi, M.; Ando, M.; Sugihara, S.; Iriyama, Y., Preparation of a visible-light-active TiO_2 photocatalyst by RF plasma treatment. *Journal of Materials Science* **2001,** *36* (17), 4201-4207.
7. Ohno, T.; Akiyoshi, M.; Umebayashi, T.; Asai, K.; Mitsui, T.; Matsumura, M., Preparation of S-doped TiO_2 photocatalysts and their photocatalytic activities under visible light. *Applied Catalysis A: General* **2004,** *265* (1), 115-121.
8. Hirai, T.; Suzuki, K.; Komasawa, I., Preparation and Photocatalytic Properties of Composite CdS Nanoparticles–Titanium Dioxide Particles. *Journal of Colloid and Interface Science* **2001,** *244* (2), 262-265.
9. Chatterjee, D.; Mahata, A., Demineralization of organic pollutants on the dye modified TiO_2 semiconductor particulate system using visible light. *Applied Catalysis B: Environmental* **2001,** *33* (2), 119-125.
10. Wang, J.; Ma, T.; Zhang, G.; Zhang, Z.; Zhang, X.; Jiang, Y.; Zhao, G.; Zhang, P., Preparation of novel nanometer TiO_2 catalyst doped with upconversion luminescence agent and investigation on degradation of acid red B dye using visible light. *Catalysis Communications* **2007,** *8* (3), 607-611.
11. Li, N.; Zhang, L.; Chen, Y.; Fang, M.; Zhang, J.; Wang, H., Highly Efficient, Irreversible and Selective Ion Exchange Property of Layered Titanate Nanostructures. *Advanced Functional Materials* **2012,** *22* (4), 835-841.
12. Yu, H.; Tian, B.; Zhang, J., Layered TiO_2 Composed of Anatase Nanosheets with Exposed {001} Facets: Facile Synthesis and Enhanced Photocatalytic Activity. *Chemistry – A European Journal* **2011,** *17* (20), 5499-

5502.

13. Nakahira, A.; Kubo, T.; Numako, C., TiO_2-Derived Titanate Nanotubes by Hydrothermal Process with Acid Treatments and Their Microstructural Evaluation. *ACS Applied Materials & Interfaces* **2010,** *2* (9), 2611-2616.
14. Bavykin, D. V.; Friedrich, J. M.; Walsh, F. C., Protonated Titanates and TiO_2 Nanostructured Materials: Synthesis, Properties, and Applications. *Advanced Materials* **2006,** *18* (21), 2807-2824.
15. Cai, Y.; Ye, Y.; Tian, Z.; Liu, J.; Liu, Y.; Liang, C., In situ growth of lamellar $ZnTiO_3$ nanosheets on TiO_2 tubular array with enhanced photocatalytic activity. *Physical Chemistry Chemical Physics* **2013,** *15* (46), 20203-20209.
16. Zhou, W.; Liu, H.; Boughton, R. I.; Du, G.; Lin, J.; Wang, J.; Liu, D., One-dimensional single-crystalline Ti-O based nanostructures: properties, synthesis, modifications and applications. *Journal of Materials Chemistry* **2010,** *20* (29), 5993-6008.
17. Pan, L.; Zou, J.-J.; Wang, S.; Huang, Z.-F.; Zhang, X.; Wang, L., Enhancement of visible-light-induced photodegradation over hierarchical porous TiO_2 by nonmetal doping and water-mediated dye sensitization. *Applied Surface Science* **2013,** *268* (0), 252-258.
18. Wang, W.; Lu, C.; Ni, Y.; Su, M.; Xu, Z., A new sight on hydrogenation of F and N-F doped {001} facets dominated anatase TiO_2 for efficient visible light photocatalyst. *Applied Catalysis B: Environmental* **2012,** *127* (0), 28-35.
19. Chen, D.; Jiang, Z.; Geng, J.; Wang, Q.; Yang, D., Carbon and Nitrogen co-doped TiO_2 with Enhanced Visible-Light Photocatalytic Activity. *Industrial & Engineering Chemistry Research* **2007,** *46* (9), 2741-2746.
20. Chen, Q.; Zhou, W.; Du, G. H.; Peng, L. M., Trititanate Nanotubes Made via a Single Alkali Treatment. *Advanced Materials* **2002,** *14* (17), 1208-1211.
21. Suetake, J.; Nosaka, A. Y.; Hodouchi, K.; Matsubara, H.; Nosaka, Y., Characteristics of titanate nanotube and the states of the confined sodium ions. *The Journal of Physical Chemistry C* **2008,** *112* (47), 18474-18482.
22. Kim, G.-S.; Kim, Y.-S.; Seo, H.-K.; Shin, H.-S., Hydrothermal synthesis of titanate nanotubes followed by electrodeposition process. *Korean Journal of Chemical Engineering* **2006,** *23* (6), 1037-1045.
23. Mao, Y.; Wong, S. S., Size- and Shape-Dependent Transformation of Nanosized Titanate into Analogous Anatase Titania Nanostructures. *Journal of the American Chemical Society* **2006,** *128* (25), 8217-8226.
24. Morgado Jr, E.; de Abreu, M. A. S.; Moure, G. T.; Marinkovic, B. A.; Jardim, P. M.; Araujo, A. S., Effects of thermal treatment of nanostructured trititanates on their crystallographic and textural properties. *Materials*

Research Bulletin **2007,** *42* (9), 1748-1760.

25. Qamar, M.; Yoon, C.; Oh, H.; Kim, D.; Jho, J.; Lee, K.; Lee, W.; Lee, H.; Kim, S., Effect of post treatments on the structure and thermal stability of titanate nanotubes. *Nanotechnology* **2006,** *17* (24), 5922.
26. Qian, L.; Du, Z.-L.; Yang, S.-Y.; Jin, Z.-S., Raman study of titania nanotube by soft chemical process. *Journal of Molecular Structure* **2005,** *749* (1), 103-107.
27. Kruk, M.; Jaroniec, M., Gas Adsorption Characterization of Ordered Organic−Inorganic Nanocomposite Materials. *Chemistry of Materials* **2001,** *13* (10), 3169-3183.
28. Soares, G. B.; Bravin, B.; Vaz, C. M. P.; Ribeiro, C., Facile synthesis of N-doped TiO_2 nanoparticles by a modified polymeric precursor method and its photocatalytic properties. *Applied Catalysis B: Environmental* **2011,** *106* (3–4), 287-294.
29. Asahi, R.; Morikawa, T.; Ohwaki, T.; Aoki, K.; Taga, Y., Visible-Light Photocatalysis in Nitrogen-Doped Titanium Oxides. *Science* **2001,** *293* (5528), 269-271.
30. Irie, H.; Watanabe, Y.; Hashimoto, K., Nitrogen-Concentration Dependence on Photocatalytic Activity of $TiO_{2-x}N_x$ Powders. *The Journal of Physical Chemistry B* **2003,** *107* (23), 5483-5486.
31. Rienks, E. D. L.; Bakker, J. W.; Baraldi, A.; Carabineiro, S. A. C.; Lizzit, S.; Weststrate, C. J.; Nieuwenhuys, B. E., Interaction of nitric oxide with Pt(100). A fast X-ray photoelectron spectroscopy study. *Surface Science* **2002,** *516* (1–2), 109-117.
32. Wu, Z.; Dong, F.; Zhao, W.; Wang, H.; Liu, Y.; Guan, B., The fabrication and characterization of novel carbon doped TiO_2 nanotubes, nanowires and nanorods with high visible light photocatalytic activity. *Nanotechnology* **2009,** *20* (23), 235701.
33. Hoffmann, M. R.; Martin, S. T.; Choi, W.; Bahnemann, D. W., Environmental Applications of Semiconductor Photocatalysis. *Chemical Reviews* **1995,** *95* (1), 69-96.

5. Hybrid CuO-$TiO_{2-x}Cl_x$ Heterostructured Composites for CO_2 Reduction by simulated Solar Irradiation

5.1 Introduction

TiO_2 has received much attention as an effective photocatalyst due to its strong catalytic activities, nontoxicity, corrosion resistance and chemical stability.[1] However, TiO_2 has the significant disadvantage to lead photocatalytic research fields. One is the low absorption in the visible light region due to its large band gap energy (3.2 eV) which can only absorb the ultraviolet light region. The other is the rapid recombination rate between photoinduced electrons and holes.

Various strategies have been applied to overcome these disadvantages. One of the strategies is to use doping with metal or non-metal. In particular, many works were performed on non-metal doping such as carbon[2], nitrogen[3], sulfur[4], fluorine[5], chlorine[6], iodine[7] and phosphine[8]. However, it is difficult to make a halogen doped TiO_2 because they have larger ionic radii rather than that of oxygen except for fluorine. K. Yang *et al*.[9] pointed out the electronic structure of halogen doped TiO_2 by first principle density functional theory (DFT). Another strategy is to couple with narrow bandgap semiconductor. Various narrow bandgap semiconductor nanoparticles such as PbS[10], CdSe[11], and CuO[12] were used as a photosensitizer. In particular CuO, a p-type semiconductor (E_g= 1.3 ~ 1.5 eV), is a one of the promising candidates for CO_2 reduction due to the suitable valence band maximum that lie near the CO_2/O_2 potential.[13] Such p-n heterostructured composites can enhance the stability of photocorrosion, lower recombination rate of photoinduced charge carriers and band alignment that are suitable for photocatalytic CO_2 reduction.

In this study, CuO and chlorine doped titanate are introduced to realize heterostructured composites as an efficient CO_2 reduction catalyst. First step, Cu@Cu_2O core-shell nanoparticles were successfully prepared by thermal decomposition method. Second, the uniform Cu@Cu_2O NPs and titanium tetrachloride ($TiCl_4$) were used to make CuO-$TiO_{2-x}Cl_x$ heterostructured composites. The pre-oxidation process of $TiCl_4$ in hydrophobic solvent can induce the two kinds of chlorine species: i) Cl incorporated into the lattice of TiO_2 and ii) Chlorine oxide (ClO_x) on the surface of the catalyst. A series of the CuO-$TiO_{2-x}Cl_x$ heterostructured composites were prepared depending on the amount of $TiCl_4$. Besides Their characteristics and photocatalytic activities were demonstrated by various instruments. The photocatalytic activities of CuO-

$TiO_{2-x}Cl_x$ heterostructured composites were evaluated by photocurrent density via time and CO_2 photoreduction to methane under solar light irradiation.

5.2 Experimental Section

5.2.1 Materials

Cu (I) acetate (Sigma Aldrich, 97%), Tri-n-octylamine (Alfa Aesar, 95%), Oleic acid (Sigma Aldrich, technical grade, 90%), titanium (IV) tetrachloride (1M in toluene), anhydrous toluene, acetone and ethanol (Sigma Aldrich, 99.5 %) were purchased and used as received without further purification.

5.2.2 Methods

Synthesis of Cu@Cu_2O core-shell nanoparticles A synthetic method was used by modified O'brien's method.[14] Cu (I) acetate (490.36 mg), Tri-n-octylamine (15 ml) and Oleic acid (4 ml) were loaded in 100 ml of 3-neck round bottom flask with schlink line. The stock solution was degassed in vacuum with the increase of temperature to 150 ℃ (3 ℃/min) for 30 min. The presence of oxygen or water is highly critical for the decomposition and nucleation. After increasing the temperature to 180 ℃, the solution was maintained for 30 min under N_2. The color of the solution gradually changed from forest green to clear brown, finally producing a dark brown colloid. It means that the formation of copper and oleic acid complex. After 30 min of reaction, the solution was rapidly heated to 270 ℃ and kept for an hour to synthesize uniform Cu nanoparticles. After the reaction for 1h, the solution was cooled to room temperature and centrifuged by anhydrous acetone (7000 rpm, 7 min) and dispersed in 5 ml of hexane. Finally the copper nanoparticles were precipitated by the mixture of acetone/ethanol and dispersed in 10 ml of anhydrous toluene.

Synthesis of CuO-$TiO_{2-x}Cl_x$ heterostructured composites 6 ml of Cu@Cu_2O NPs solution dispersed in toluene was loaded in 20 ml of rubber capped vial and degassed for 30 min under vacuum to remove O_2 dissolved in the solution and fully filled with the inert gas (Ar). The degassed solution was transferred into the glove box, and a certain amount of 1M titanium (IV) chloride solution (The volume of $TiCl_4$= 0.3, 0.5, 0.7, and 0.9 ml) was added dropwise to degassed solution. The color was changed from dark

green to dark yellow. After 1 h reaction, a well dispersed Cu@Cu_2O NPs and $TiCl_4$ mixed solution with dark yellow was released into outside, and open the rubber cap to oxidize mixture spontaneously for 30 min with stirring and air blowing. The color of the mixture was changed from dark yellow to reddish brown. A solvent was removed on alumina boat at 70 ℃ in the air. Completely dried sample was calcined in a tubular furnace at 400 ℃ with the ramping rate of 6 ℃ / min for 3 h. The obtained materials were labeled as CT03, CT05, CT07, and CT09 for the sample obtained with 0.3, 0.5, 0.7, and 0.9 ml of $TiCl_4$, respectively.

Photocatalytic CO_2 reduction test The photocatalytic CO_2 reduction experiment with H_2O for various catalysts were performed as reported earlier.[15] Prior to the experiments, the photoreactor which was newly designed by our research was purged with vacuum. Before the photocatalyst loading, the reactor was purged with CO_2 gas about 3 times in order to remove any air or other impurities present in the system. 1,000 ppm of high purity CO_2 gas was passed through a water bubbler to allow a mixture of CO_2 and H_2O vapor. A 100W Xenon solar simulator (Oriel, LCS-100) with an AM1.5 filter was used as a light source. For each test, 100 mg of samples were reacted for 1 h under CO_2 atmosphere with H_2O vapor and the product was analyzed by gas chromatograph.

5.2.3 Analysis

Ultraviolet-Visible-Near Infrared Diffuse Reflectance Spectroscopy (UV-Vis-NIR DRS). All the absorption spectra of the samples were obtained by a UV-Vis-NIR spectrophotometer (Agilent Technologies, Cary 5000).

X-ray Diffraction Analysis (XRD). The XRD patterns were obtained using X-Ray Diffractometer (Rigaku, MiniFlex 600/300).

Transmission Electron Microscopy (TEM). The TEM images were obtained by FE-TEM (Hitachi HF-3300) instrument operating at 300 kV.

X-ray Photoelectron Spectroscopy (XPS). X-ray photoelectron spectra were obtained using an ESCALAB 250Xi operated by Ki-Hee Kim, CCRF of DGIST.

Gas Chromatography (GC). Gas Chromatogram was carried out by Shimadzu GC-2014 (Restek Rt-Q-Bond column, ID=0.53 mm, length=30 m) equipped with a thermal conductivity detector (TCD) and a flame ionization detector (FID).

5.3 Results & Discussion

A synthetic strategy in this experiment is to couple p-type semiconductor (CuO) with Cl doped n-type semiconductor ($TiO_{2-x}Cl_x$) to enhance the photocatalytic CO_2 reduction activity by increasing charge separation rate, absorption range, and CO_2 selectivity. The $Cu@Cu_2O$ core-shell nanoparticles were successfully synthesized by thermal decomposition as a CuO precursor.

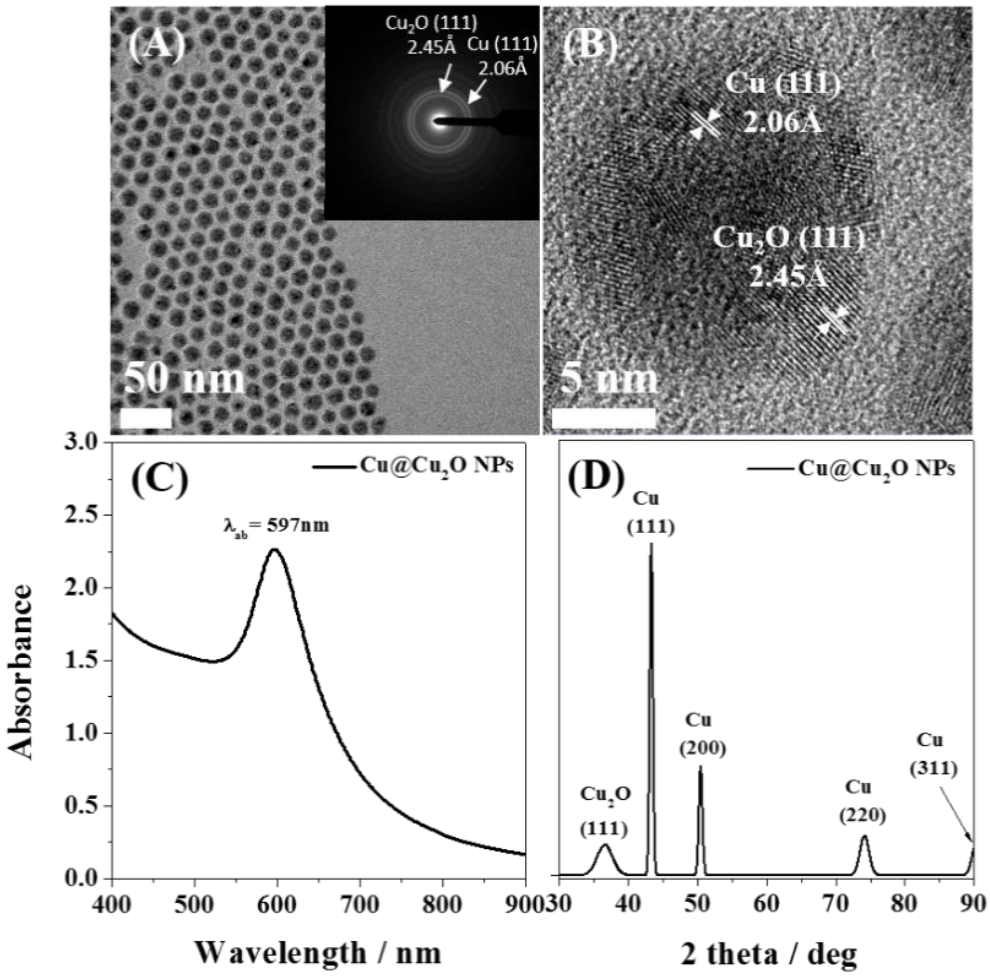

Figure 5. 1 (A) TEM and SAED (inset) images, (B) HR-TEM image, (C) UV-Vis absorption spectra and (D) XRD pattern analysis of $Cu@Cu_2O$ core-shell nanoparticles

Figure 5.1A shows the transmission electron microscope (TEM) images of well dispersed Cu@Cu_2O core-shell nanoparticles and selected area electron diffraction (SAED) pattern (inset). The SAED pattern shows the polycrystalline of Cu@Cu_2O nanoparticles by clear circles of Cu (111) and Cu_2O (111). The average size of Cu@Cu_2O nanoparticles was observed in the range of 14-15 nm. In Figure 5.1B, the particles were composed of metallic Cu core and Cu_2O shell as confirmed by the lattice distance and SAED pattern. It shows the lattice distance of Cu (d_{111}, 2.06 Å) and Cu_2O (d_{111}, 2.45 Å). UV-Visible absorption spectrum is shown in Figure 5.1C. The surface plasmonic absorption of Cu@Cu_2O nanoparticles appeared narrow peak at the wavelength of 596 nm.[16] It suggests that the solution has a narrow size distribution which is corresponding to the result of TEM image. X-ray diffraction pattern analysis was performed to identify its crystallinity. The as-prepared sample shows diffraction peaks at 2θ values of 36.7 º 43.4 º, 50.5 º, 74.1 º and 90.0 º in Figure 5.1D. The small peak at 36.7 º is a (111) plane of Cu_2O cubic crystal structure and the other peaks are corresponding with d_{111}, d_{200}, d_{220}, d_{311} of Cu cubic crystal structure, respectively, indicating the presence of Cu (JCPDF no. 85-1326) and Cu_2O (JCPDF no. 78-2076) phase. This Cu_2O phase is formed at the precipitation process. After the precipitation, the copper nanoparticles were dispersed in anhydrous toluene and exposed in the air. The color of Cu nanoparticles were immediately changed from dark red to dark green by the spontaneous oxidation to Cu_2O. The TEM and HR-TEM images of CuO-$TiO_{2-x}Cl_x$ heterostructured composites are shown in Figure 5.2 A and B.

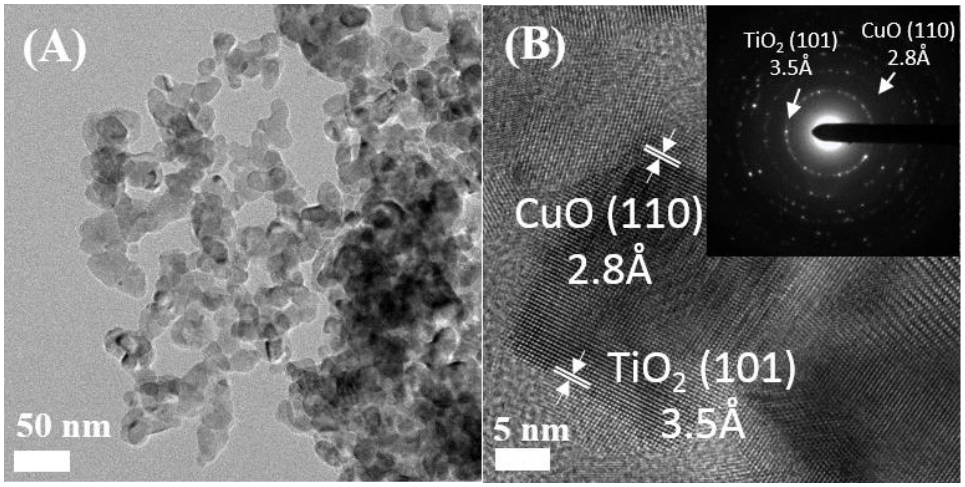

Figure 5. 2 (A) Transmission Electron Microscopy (TEM), (B) high resolution-TEM and SAED (inset) images of CuO-$TiO_{2-x}Cl_x$ heterostructured composites.

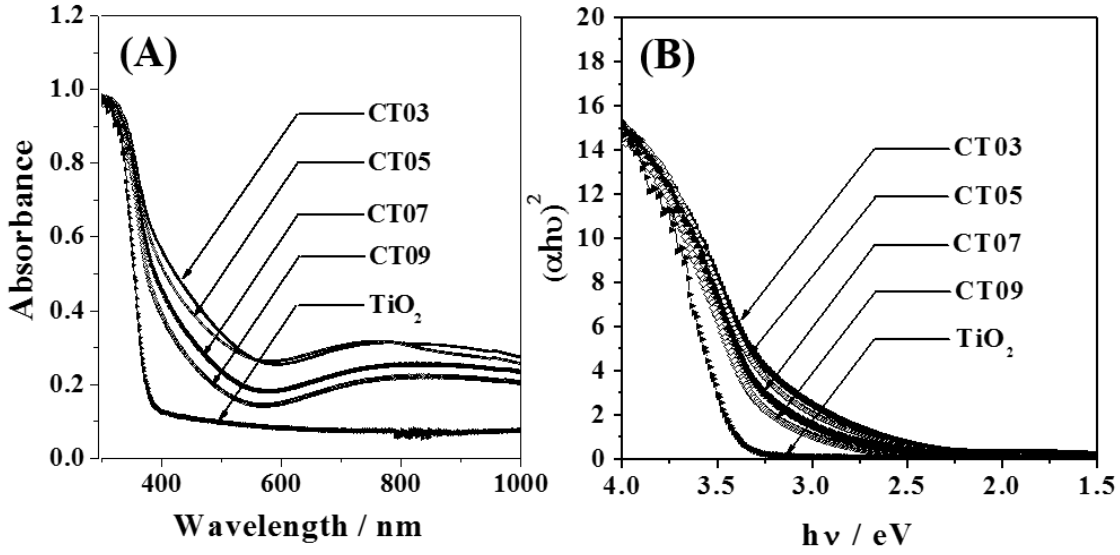

Figure 5. 3 (A) UV-Visible diffuse reflectance spectroscopy (DRS) and (B) calculated tauc plot of CuO-$TiO_{2-x}Cl_x$ heterostructured composites.

It can be clearly seen that CuO and TiO_2 appears in well aggregated structure resulting in the formation of CuO-$TiO_{2-x}Cl_x$ heterostructured composites. The p-n heterojunction formed at the interface between TiO_2 and CuO. The SAED pattern (inset) indicates the crystallinity of monoclinic CuO and tetragonal TiO_2 with the lattice distance of high-resolution images. Figure 5.3 shows the UV-Vis diffuse reflectance spectra (UV-Vis DRS) and Tauc transformation plot to observe light absorption and bandgap of pure-TiO_2 and a series of CuO-$TiO_{2-x}Cl_x$ composites. The bandgap energy for each samples displayed in Table 5. 1. The bandgap energy of CuO-$TiO_{2-x}Cl_x$ composites were reduced by coupling with CuO and Cl doping on the TiO_2. Pure TiO_2 did not absorb visible light due to the large band gap (3.2~3.3eV) whereas a series of CuO-$TiO_{2-x}Cl_x$ composites appeared two characteristic absorption in the visible light region. First, the light absorption was enhanced from the 400 nm to 500 nm, which is caused by non-metal doping and CuO effect. However, when the amount of $TiCl_4$ was increased, the light absorption near 400 nm to 500 nm was decreased. The reason why the absorption near 400 nm reduced with the increase of Cl precursor may related with relative CuO and Cl doping contents. The ratio of CuO increased with the decrease of Cl precursor, respectively. It means that the absorption by CuO near 400 nm is increased when the amount of Cl precursor increased. This extended absorption enhancement above 400 nm indicates that an interfacial charge transfer from O 2p valence band to Cu^{2+} state.[17]

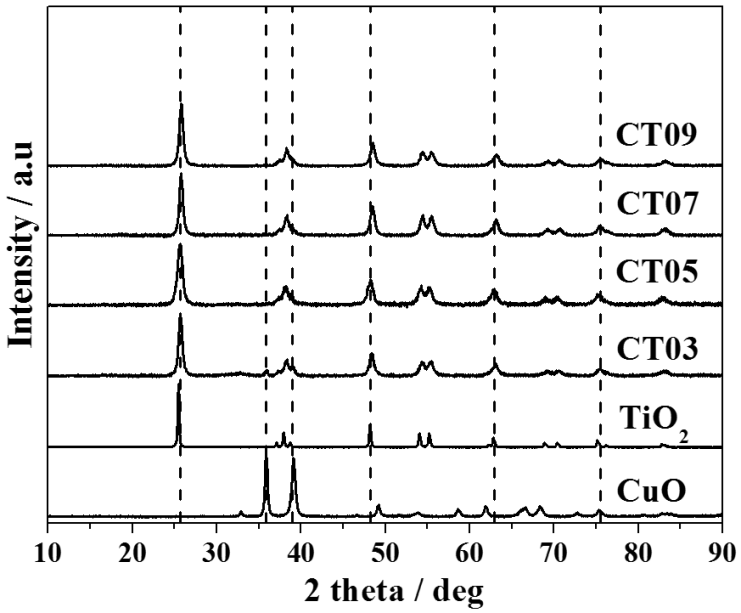

Figure 5. 4 XRD pattern analysis for a series of CuO-$TiO_{2-x}Cl_x$ composites with pure-CuO and TiO_2 as reference.

Qiu *et al.*[18] suggests that the absorption enhancement above 400 nm shows due to charge transfer from TiO_2 to CuO in a system of CuO-TiO_2 composites. In addition, the absorption enhancement near 400 nm is also shown by Cl doping.[6] So, it is very difficult to distinguish an absorption enhancement factor, because this absorption above 400 nm was enhanced by two kinds of factor: i) the absorption of CuO and ii) Cl doping. Second, the broad absorption region extending 600 nm to 1000 nm by CuO were shown. These broad absorption was enhanced with the increase of the CuO ratio, respectively. It mainly comes from the *d-d* transition of Cu^{2+} in the crystalline TiO_2 system.[17]

The X-ray powder diffraction was used to determine the crystalline phase of as-prepared samples. XRD pattern of CuO-$TiO_{2-x}Cl_x$ composites are shown in Figure 5.4. Almost peaks of as-prepared samples were readily indexed to anatase TiO_2. The peaks at 25.8°, 38.2° and 48.3° was attributed to (101), (004) and (200) plane of anatase TiO_2, respectively. The amount of CuO does not have any effect on the crystallinity of TiO_2.The broad region at 38.7° and small peak at 75.2° were from monoclinic CuO (111) and (22-2) lattice plane. The peak of CuO (11-1) plane at 35.5° was only observed in CT03 which have highest relative CuO ratio.

To investigate the oxidation state of each element, the x-ray photoelectron spectroscopy (XPS) was performed for CuO-$TiO_{2-x}Cl_x$ composites in Figure 5.5. The binding energy of Ti $2p_{3/2}$ and $2p_{1/2}$ was observed at 458.0 eV and 463.9 eV in Figure 5.5A. The binding energy of Ti $2p_{3/2}$ (458.0 eV) for CT07 was decreased than that of other literature TiO_2 (458.5~459.0 eV).[19] It is caused by different electronic state of Ti^{4+} with anions (Cl^-) which cause electron transfer from Cl 2p to Ti 3d orbital and an increase of electron density of Ti^{4+} due to lower electron negativity of Chlorine compared with oxygen. This result proved that Chlorine was incorporated into the lattice of TiO_2 and substituted for oxygen.[20]

Figure 5.5B shows that the photoelectron peaks of Cu $2p_{3/2}$ and Cu $2p_{1/2}$ was around 932.8 eV and 952.8 eV, which indicates the presence of Cu^{2+}.[21] In here, the slight peak shift occurred to lower binding energy compared with the reference data and other literature value related with that of CuO (933.4~933.9 eV).[22, 23] The presence of satellite peaks near 942.5 eV and 962 eV appeared in Cu 2p spectra which have been attributed to shake-up transition by ligand to metal charge transfer was used as an indication of the presence of Cu^{2+} species.[24] These charge transfer were not occurred in Cu^+ or metallic Cu^0 species due to their completely filled 3d shells.

The XPS spectra of the C 1s region in Figure 5.5C was convoluted into three kinds of peaks at 284.5, 286.5, and 288.8 eV. These peaks are corresponding with the C-C, C-O and C=O bonds, respectively.[25] It may come from organic impurities on the surface of CuO-$TiO_{2-x}Cl_x$ composites. The O 1s region shown in Figure 5.5D was also convoluted to 3 peaks at 529.3, 530.3, and 531.7 eV, which are attributed to the oxygen in Cu-O, Ti-O bonding and hydroxyl oxygen atoms.[26, 27] The Cl 2p region of CuO-$TiO_{2-x}Cl_x$ composites are shown in Figure 5.5E. The Cl 2p peaks are split into two kinds of peak at 198.4 and 200.5 eV with Gaussian fitting. The minor contribution at 198.4 eV is the anionic Cl ion incorporated into the TiO_2 lattice via O-Ti-Cl bonding and major contribution at 200.5 eV come from chemisorbed Chlorine.[27, 28]

The Cl 2p peaks of a series of CuO-$TiO_{2-x}Cl_x$ are shown in Figure 5.5F. The amount of dopant increased with the increase of $TiCl_4$, but the amount of dopant ion decreased when an excess amount of $TiCl_4$ (CT09) were added. These XPS results confirmed that the chlorine was doped into the lattice of TiO_2 by the direct oxidation of $TiCl_4$ in a hydrophobic solvent such as toluene and CuO was successfully loaded on the surface of TiO_2 from the Cu@Cu_2O core-shell nanoparticles by heating.

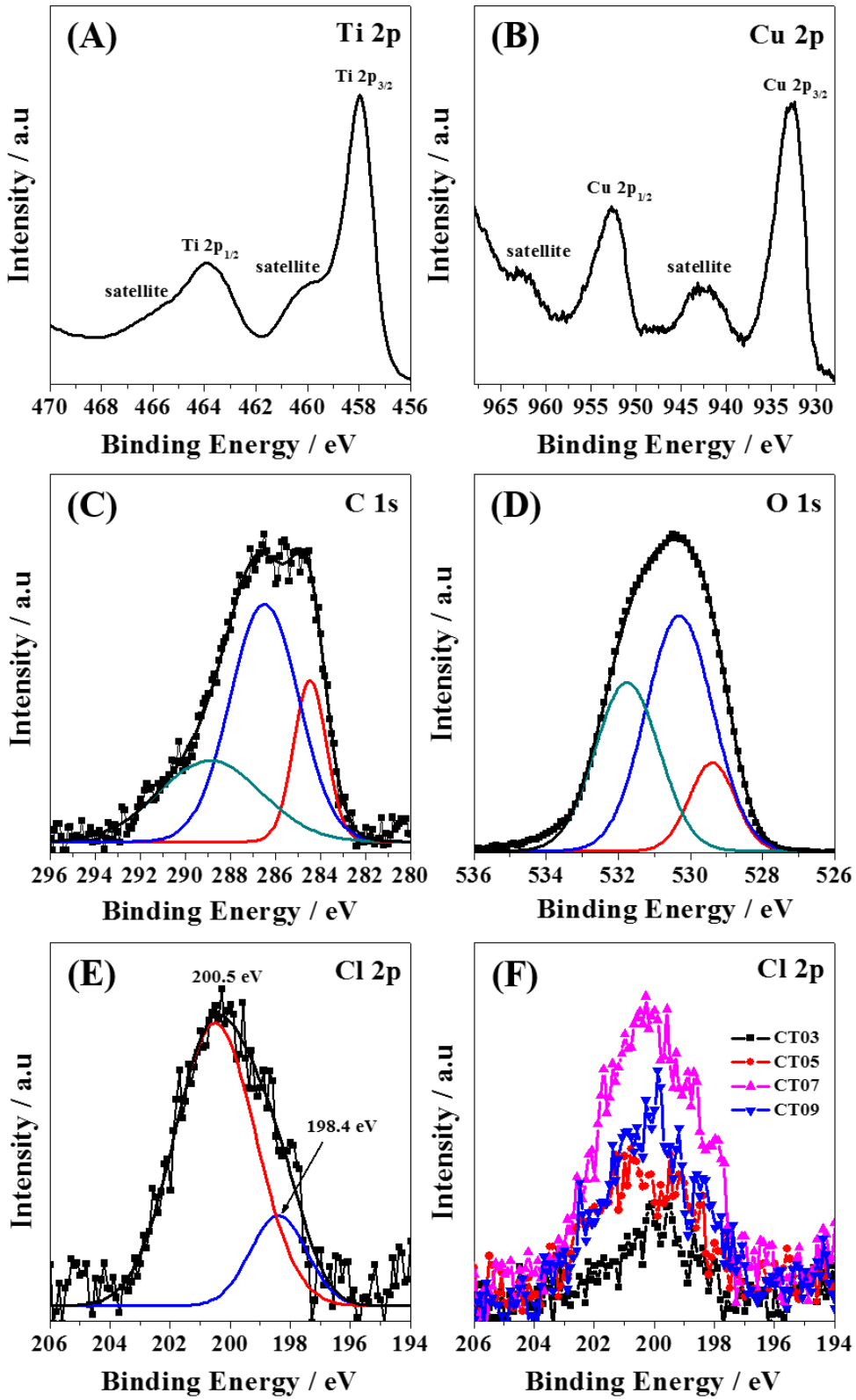

Figure 5. 5 XPS spectra for (A) Ti 2p, (B) Cu 2p, (C) C 1s, (D) O 1s and (E) Cl 2p region of CT07, and (F) Cl 2p region of a series of CuO-$TiO_{2-x}Cl_x$ composites.

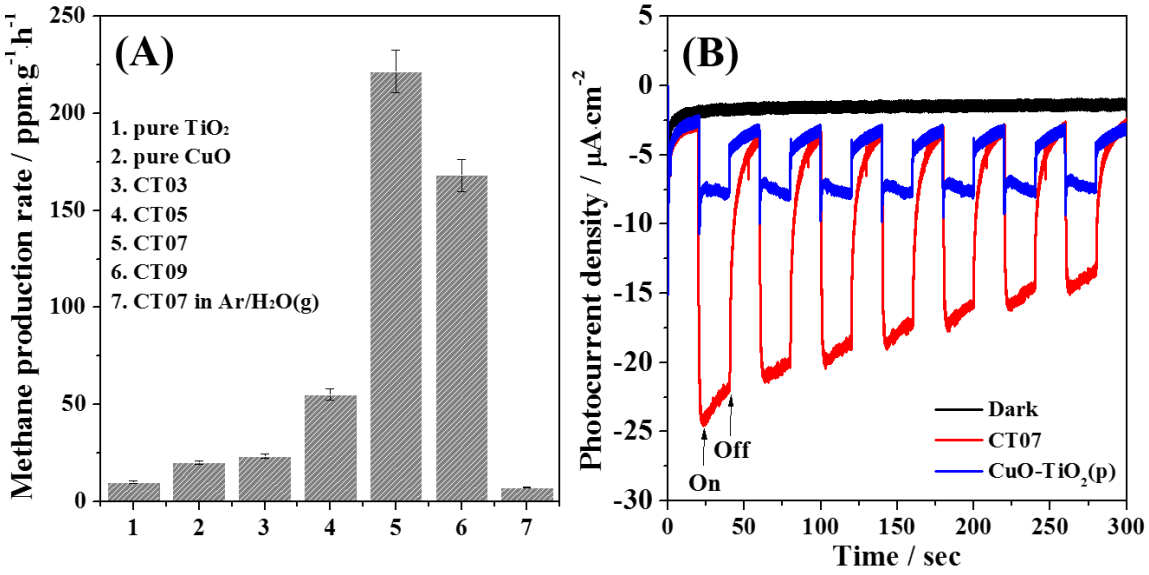

Figure 5. 6 (A) Photocatalytic CO_2 reduction by gas chromatogram (GC) and (B) Time-resolved photocurrent density via time in 1M Na_2SO_4 solution at 0 V vs. Ag/AgCl reference electrode. The electrochemical cell of CuO-$TiO_{2-x}Cl_x$ composites was irradiated by AM 1.5G simulated solar simulator.

The Brunauer-Emmett-Teller (BET) specific surface area analysis was introduced to identify the specific surface area of the as-prepared samples. The result of BET specific surface area of the CuO-$TiO_{2-x}Cl_x$ samples are displayed in Table 5.1, respectively. Among all the samples, CT07 shows highest surface area (26.946 $m^2 \cdot g^{-1}$) which is about 2.4 times higher than that of CT03 (11.053 $m^2 \cdot g^{-1}$). Upon increasing the $TiCl_4$ amount, its surface area of CT09 becomes lower than that of CT07. This can be attributed to the aggregation due to increase of Ti precursor.

Photocatalytic CO_2 reduction performance of CuO-$TiO_{2-x}Cl_x$ hetero-structured composites were carried out by gas chromatography (GC) under simulated solar irradiation at ambient temperature. CuO, purchased at Sigma Aldrich, and TiO_2 made by same experimental procedure without Cu@Cu_2O core-shell nanoparticles were used as a reference sample. The major product produced by photocatalytic CO_2 reduction showed preferentially methane along with ethane as a minor product under 1 h irradiation. Figure 5.6A shows the methane production rate for each samples. When CuO was coupled with $TiO_{2-x}Cl_x$ to have heteostructured p-n junction, its system shows dramatic enhancement of CO_2 reduction to hydrocarbon. CT07 shows highest value of methane production (221.63 $ppm \cdot g^{-1} \cdot h^{-1}$, or 8.816 $\mu mol \cdot g^{-1} \cdot h^{-1}$) which is 10.1 times and 22 times faster than that of CuO (20.01 $ppm \cdot g^{-1} \cdot h^{-1}$) and TiO_2 (9.94 $ppm \cdot g^{-1} \cdot h^{-1}$) under the same conditions.

This value is higher than that of previous research for CuO-$TiO_{2-x}N_x$[12], CdS/TiO_2[29], and $CdSe/Pt/TiO_2$[11]. The CO_2 reduction efficiency was enhanced with the increase of dopant ions from CT03 to CT07.

In case of CT09, the methane production rate was lower than that of CT07. This trend is corresponding with that of XPS result. To identify the carbon source of product, CT07 was illuminated in the Ar/H_2O (g) atmosphere under simulated 1 sun irradiation. It shows negligible photocatalytic activity, suggesting that some organic impurities adsorbed on the surface of CuO-$TiO_{2-x}Cl_x$ have negligible involvement in the photocatalytic CO_2 reduction reaction. There are two kinds of factors for the enhancement of photocatalytic CO_2 reduction: i) Cu species directing the selectivity toward to CO_2 and harvesting visible light. CuO enhanced the visible light absorption in the range of above 400 nm and 600 nm to 1000 nm which can provide enough photogenerated electrons to reduce CO_2 into methane. In addition, Cu species have high selectivity for CO_2 to increase adsorption rate on the surface of catalyst. ii) Cl doping to enhance visible light absorption. Cl incorporated TiO_2 shows the absorption enhancement above 400 nm. It suggest that the photogenerated electrons can more easily be participated in the reaction of CO_2 reduction.

To investigate the photoresponse of CuO-$TiO_{2-x}Cl_x$ under 1 sun condition, a photocurrent density of CuO-$TiO_{2-x}Cl_x$ heterostructured composites was carried out by measuring the current vs. time with a three electrode system at a potential (V) of 0 V vs. Ag/AgCl reference electrode. The photocurrent density (I) generated in the CT07 catalyst (CuO-$TiO_{2-x}Cl_x$ by 0.7 ml of $TiCl_4$) is shown in Figure 5.6B. In comparison to CuO-TiO_2 made by physisorption, the current density of CT07 at pH=7.04 was approximately 3 times higher than that of CuO-TiO_2 made by physisorption process. However, the photostability of CT07 is approximately 30% decreased compared to initial value. This result shows that the p-n heterojunction structure was successfully formed and charge collection was better than physisorbed CuO-TiO_2.

Table 5. 1 BET specific surface area, pore volume, bandgap energy and the value of photocatalytic CH_4 production rate for a series of CuO-$TiO_{2-x}Cl_x$ composites.

Materials	S_{BET} ($m^2 \cdot g^{-1}$)[a]	Pore Volume ($cm^3 \cdot g^{-1}$)[b]	Bandgap E (eV)[c]	Amount of CH_4 ($ppm \cdot g^{-1} \cdot h^{-1}$)
CT03	11.053	0.115	3.096	23.33
CT05	16.494	0.102	3.12	55.07
CT07	26.946	0.094	3.15	221.63
CT09	22.953	0.164	3.2	168.03

[a] Surface area determined by applying Brunauer-Emmett-Teller (BET) equation to a relative pressure (P/P_0) range of 0.05-0.35 of the adsorption isotherm.

[b] Pore diameter is calculated from the Barrett-Joyner-Halenda (BJH) equation using the desorption isotherm.

[c] Band gap energies estimated from Tauc plots.

5.4 Conclusions

In summary, Cu_xO-$TiO_{2-x}Cl_x$ heterostructured composites were prepared by using Cu@Cu_2O core-shell nanoparticles and $TiCl_4$ with simple synthetic method. The as-prepared samples were characterized by various equipment such as UV-Vis DRS, XPS, TEM, STEM and BET. A p-n heterojunction structure was successfully realized by heat treatment under air atmosphere and chlorine was incorporated into the lattice of TiO_2 by $TiCl_4$ in hydrophobic solvent (toluene) under simultaneous oxidation. A bandgap reduction of as-prepared samples are observed to couple with CuO and Cl doping, which is due to the Cl 2p states above the valence band maximum. The photocatalytic CO_2 reduction activity of Cu_xO-$TiO_{2-x}Cl_x$ heterostructured composites shows dramatically enhanced CO_2 reduction efficiency (221.63 $ppm \cdot g^{-1} \cdot h^{-1}$, or 8.816 $\mu mol \cdot g^{-1} \cdot h^{-1}$). The trend of photocatalytic CO_2 reduction is corresponding with that of the amount of dopant ions and BET specific surface area. The enhancement of photocatalytic CO_2 reduction performance might be due to the broadening absorption range in the visible light region by Cl doping and CuO coupling, enhanced specific surface area, and effective charge separation from p-n heterojunction.

5.5 References

1. Linsebigler, A. L.; Lu, G.; Yates, J. T., Photocatalysis on TiO_2 Surfaces: Principles, Mechanisms, and Selected Results. *Chemical Reviews* **1995,** *95* (3), 735-758.
2. Ren, W.; Ai, Z.; Jia, F.; Zhang, L.; Fan, X.; Zou, Z., Low temperature preparation and visible light photocatalytic activity of mesoporous carbon-doped crystalline TiO_2. *Applied Catalysis B: Environmental* **2007,** *69* (3–4), 138-144.
3. Sathish, M.; Viswanathan, B.; Viswanath, R. P.; Gopinath, C. S., Synthesis, Characterization, Electronic Structure, and Photocatalytic Activity of Nitrogen-Doped TiO_2 Nanocatalyst. *Chemistry of Materials* **2005,** *17* (25), 6349-6353.
4. Yu, J. C.; Ho, W.; Yu, J.; Yip, H.; Wong, P. K.; Zhao, J., Efficient Visible-Light-Induced Photocatalytic Disinfection on Sulfur-Doped Nanocrystalline Titania. *Environmental Science & Technology* **2005,** *39* (4), 1175-1179.
5. Yu, J. C.; Yu, H.; Jiang, Z., Effects of F-doping on the Photocatalytic Activity and Microstructures of Nanocrystalline TiO_2 Powders. *Chemistry of Materials* **2002,** *14* (9), 3808-3816.
6. Xu, H.; Zheng, Z.; Zhang, L.; Zhang, H.; Deng, F., Hierarchical chlorine-doped rutile TiO_2 spherical clusters of nanorods: Large-scale synthesis and high photocatalytic activity. *Journal of Solid State Chemistry* **2008,** *181* (9), 2516-2522.
7. Liu, G.; Chen, Z.; Dong, C.; Zhao, Y.; Li, F.; Lu, G. Q.; Cheng, H.-M., Visible Light Photocatalyst: Iodine-Doped Mesoporous Titania with a Bicrystalline Framework. *The Journal of Physical Chemistry B* **2006,** *110* (42), 20823-20828.
8. Lin, L.; Lin, W.; Zhu, Y.; Zhao, B.; Xie, Y., Phosphor-doped Titania - A Novel Photocatalyst Active in Visible Light. *Chemistry Letters* **2005,** *34* (3), 284-285.
9. Yang, K.; Dai, Y.; Huang, B.; Whangbo, M.-H., Density Functional Characterization of the Band Edges, the Band Gap States, and the Preferred Doping Sites of Halogen-Doped TiO_2. *Chemistry of Materials* **2008,** *20* (20), 6528-6534.
10. Wang, C.; Thompson, R. L.; Ohodnicki, P.; Baltrus, J.; Matranga, C., Size-dependent photocatalytic reduction of CO_2 with PbS quantum dot sensitized TiO_2 heterostructured photocatalysts. *Journal of Materials Chemistry* **2011,** *21* (35), 13452-13457.

11. Wang, C.; Thompson, R. L.; Baltrus, J.; Matranga, C., Visible light photoreduction of CO_2 using CdSe/Pt/TiO_2 heterostructured catalysts. *The Journal of Physical Chemistry Letters* **2009,** *1* (1), 48-53.

12. In, S. I.; Vaughn, D. D.; Schaak, R. E., Hybrid CuO-$TiO_{2-x}N_x$ Hollow Nanocubes for Photocatalytic Conversion of CO_2 into Methane under Solar Irradiation. *Angewandte Chemie International Edition* **2012,** *51* (16), 3915-3918.

13. Roy, S. C.; Varghese, O. K.; Paulose, M.; Grimes, C. A., Toward Solar Fuels: Photocatalytic Conversion of Carbon Dioxide to Hydrocarbons. *ACS Nano* **2010,** *4* (3), 1259-1278.

14. Yin, M.; Wu, C.-K.; Lou, Y.; Burda, C.; Koberstein, J. T.; Zhu, Y.; O'Brien, S., Copper oxide nanocrystals. *Journal of the American Chemical Society* **2005,** *127* (26), 9506-9511.

15. Hye Rim, K.; Abdul, R.; Hyo Jung, H.; Su-Il, I., Photocatalytic conversion of CO_2 into hydrocarbon fuels with standard titania using newly installed exerimental setup. *Rapid Communication in Photoscience* **2013,** *2* (2), 64-66.

16. Hung, L. I.; Tsung, C. K.; Huang, W.; Yang, P., Room-Temperature Formation of Hollow Cu_2O Nanoparticles. *Advanced Materials* **2010,** *22* (17), 1910-1914.

17. Choudhury, B.; Dey, M.; Choudhury, A., Defect generation, d-d transition, and band gap reduction in Cu-doped TiO_2 nanoparticles. *Int Nano Lett* **2013,** *3* (1), 1-8.

18. Qiu, X.; Miyauchi, M.; Sunada, K.; Minoshima, M.; Liu, M.; Lu, Y.; Li, D.; Shimodaira, Y.; Hosogi, Y.; Kuroda, Y.; Hashimoto, K., Hybrid Cu_xO/TiO_2 Nanocomposites As Risk-Reduction Materials in Indoor Environments. *ACS Nano* **2011,** *6* (2), 1609-1618.

19. Huang, Q.; Kang, F.; Liu, H.; Li, Q.; Xiao, X., Highly aligned $Cu_2O/CuO/TiO_2$ core/shell nanowire arrays as photocathodes for water photoelectrolysis. *Journal of Materials Chemistry A* **2013,** *1* (7), 2418-2425.

20. Wang, X.-K. W., Chen. Zhang, Dan, Sonochemical synthesis and characterization of Cl–N-codoped TiO_2 nanocrystallites. *Materials Letters* **2012,** *72* (0), 12-14.

21. You, M.; Kim, T. G.; Sung, Y.-M., Synthesis of Cu-doped TiO_2 nanorods with various aspect ratios and dopant concentrations. *Crystal Growth & Design* **2009,** *10* (2), 983-987.

22. Wang, Z.; Liu, Y.; Martin, D. J.; Wang, W.; Tang, J.; Huang, W., CuO_x–TiO_2 junction: what is the active component for photocatalytic H_2 production? *Physical Chemistry Chemical Physics* **2013,** *15* (36), 14956-14960.

23. C. D. Wanger; W. M. Riggs; L. E. Davis; Moulder, J. F.; E.Muilenberg, G., Handbook of X-ray Photoelectron

Spectroscopy Perkin-Elmer Corp., Physical Electronics Division, Eden Prairie, Minnesota, USA, . *Surface and Interface Analysis* **1981,** *3* (4).

24. Li, P.; Wang, H.; Xu, J.; Jing, H.; Zhang, J.; Han, H.; Lu, F., Reduction of CO_2 to low carbon alcohols on CuO FCs/Fe_2O_3 NTs catalyst with photoelectric dual catalytic interfaces. *Nanoscale* **2013,** *5* (23), 11748-11754.
25. How, G. T. S.; Pandikumar, A.; Ming, H. N.; Ngee, L. H., Highly exposed {001} facets of titanium dioxide modified with reduced graphene oxide for dopamine sensing. *Scientific Reports* **2014,** *4*, 5044.
26. Dubal, D. P.; Gund, G. S.; Holze, R.; Jadhav, H. S.; Lokhande, C. D.; Park, C.-J., Surfactant-assisted morphological tuning of hierarchical CuO thin films for electrochemical supercapacitors. *Dalton Transactions* **2013,** *42* (18), 6459-6467.
27. Wang, X.-K.; Wang, C.; Jiang, W.-Q.; Guo, W.-L.; Wang, J.-G., Sonochemical synthesis and characterization of Cl-doped TiO_2 and its application in the photodegradation of phthalate ester under visible light irradiation. *Chemical Engineering Journal* **2012,** *189–190* (0), 288-294.
28. Xu, H.; Zhang, L., Selective Nonaqueous Synthesis of C− Cl-codoped TiO_2 with Visible-Light Photocatalytic Activity. *The Journal of Physical Chemistry C* **2010,** *114* (26), 11534-11541.
29. Ahmad Beigi, A.; Fatemi, S.; Salehi, Z., Synthesis of nanocomposite CdS/TiO_2 and investigation of its photocatalytic activity for CO_2 reduction to CO and CH_4 under visible light irradiation. *Journal of CO_2 Utilization* **2014,** *7* (0), 23-29.

6. Conclusions

The Solar Energy materials to convert carbon dioxide (CO_2) into hydrocarbon fuels such as methane (CH_4), methanol (CH_3OH), ethane (C_2H_6) and so on was studied to solve the energy problem that we are facing. Photocatalytic reduction process of CO_2 is an innovative breakthrough to find a solution for both energy crisis and environmental pollution.

First, the carbon and nitrogen co-doped sodium titanate nanotubes (C, N-TNT) was developed as effective solar light photocatayst to convert CO_2 into methane. The C and N which are from urea was incorporated into the lattice of TNT by calcination. It showed the effective photocatalytic activities for dye degradation and CO_2 reduction. The C, N-TNT1 exhibits the highest rate constant of 0.00701 min^{-1} which is 2.5 times higher as compared to bare-TNT for MB dye degradation. The C, N-TNT06 shows the highest CH_4 evolution (9.75 μmol/g, 1 h irradiation), which is about 2.7 times higher than that of bare TNT (3.7 μmol/g, 1 h irradiation).

Second, Copper oxide and Chlorine doped titanate ($CuO\text{-}TiO_{2-x}Cl_x$) heterostructured composites were successfully synthesized by a simple novel synthetic method. The absorption in the Visible light region above 400 nm was enhanced by the charge transfer from TiO_2 to CuO and Cl doping effect in TiO_2. The broad absorption range from 600 nm to 1000 nm was also enhanced by the *d-d* transition of Cu^{2+} in CuO. Chlorine doping was identified by x-ray photoelectron spectroscopy (XPS) and CT07 shows highest peak intensity in Cl 2p region. The photocatalytic CO_2 reduction of $CuO\text{-}TiO_{2-x}Cl_x$ was estimated by gas chromatography. The CT07 shows highest CH_4 production rate (221.63 $ppm \cdot g^{-1} \cdot h^{-1}$, or 8.816 $\mu mol \cdot g^{-1} \cdot h^{-1}$) under simulated solar irradiation. There are many factors such as visible light absorption, CO_2 selectivity of CuO, and enhanced the specific surface area was related to the enhancement of photocatalytic activity.

The energy storage and environmental problems are becoming the great challenging for human in this century. The photocatalytic CO_2 reduction to usable hydrocarbon fuels is a promising field to solve global energy problem. The goal is to synthesize photoactive materials having high conversion efficiency and selectivity that exceeds the nature's photosynthesis. Furthermore, it may innovate if the photcatalyst are operated under weak indoor light. However, it is very hard to realize efficient photocatalyst because photoreduction of CO_2 is thermodynamically uphill and multi-electron reaction. So we need a longstanding strategy through the convergence with various fields of catalysis, energy science, physics, biology and green chemistry.

요 약 문

태양빛을 이용한 이산화탄소의 탄화수소연료 전환을 위한 융합형 광촉매 시스템의 연구

최근 인류는 무분별한 화석연료의 사용에 의해 에너지 부족현상 및 환경오염등과 같은 문제 때문에 직면하고 있다. 화석연료는 안정성 및 높은 에너지 밀도 때문에 가장 중요한 에너지원 중 하나이다. 하지만 화석연료의 사용은 대기 중의 이산화탄소의 농도를 증가시키며, 다양한 형태의 환경오염을 유발할 수 있다. 이러한 환경오염에는 주로 온실효과에 의한 지구 온난화, 대기오염, 해수면 상승 등이 있다. 특히 지구 온난화는 대기 중의 이산화탄소와 밀접한 연관이 있다.

대기 중 이산화탄소의 농도와 지구 온도의 관계를 살펴보면 비례관계라는 것을 확인 할 수 있다. 전세계적으로 인류는 12 일당 10 억배럴의 화석연료를 소비하고 있으며 이는 1 조 파운드의 이산화탄소에 해당하는 양이다. 이렇게 엄청난 양의 이산화탄소가 대기 중으로 배출되면, 온실가스로써 이산화탄소는 극심한 지구 온난화를 유발하게 된다. 또한 과도한 화석연료의 사용은 지구상에 존재하는 에너지원의 고갈을 초래하고 에너지부족현상을 야기한다.

이렇게 현재 대두되고 있는 에너지원에 대한 문제 및 이산화탄소에 의한 지구온난화를 동시에 해결할 수 있는 것이 바로 태양광을 이용한 촉매이다. 광촉매 라고 불리는 물질은 태양광을 이용하여 이산화탄소를 인류가 사용할 수 있는 연료로 전환할 수 있으며, 물을 분해하여 수소와 산소를 얻고, 오염물질을 분해할 수 있다. 이에 따라 광촉매를 이용한 이산화탄소 전환연구는 이러한 수요를 충족시킬 수 있는 촉망 받는 연구 중 하나이다. 광촉매를 이용하여 이산화탄소를 사용 가능한 연료로 전환시킴으로써, 대기 중에 존재하는 이산화탄소의 농도를 감소시키고 지구온난화 효과를 억제할 수 있을 뿐만 아니라 메탄, 에탄, 메탄올 같은 짧은 고리의 유기화합물을 생성함에 따라 연료수급 문제 및 기타 유기화합물 제조에도 큰 기여를 할 수 있다.

게다가 이산화탄소는 지구상에 상당량 존재하는 물질로써 탄소순환이 가능하며 태양광 또한 무한한 에너지원이기에 친환경적인 방법으로 에너지를 생산할 수 있다.

이러한 장점에도 불구 하고 이산화탄소 전환용 광촉매에 대한 연구가 아직까지 실험단계에 머무르고 있는 이유는 낮은 광전환률 및 선택성 때문이다. 물 분해반응의 경우, 두 개의 전자가 반응에 참여하며 간단한 반응에 의해 상대적으로 쉽게 일어나지만, 메탄 또는 기타 탄소유도체 생성반응은 2개부터 8개까지 다수의 전자가 반응에 참여할 뿐만 아니라 여러 단계의 반응이 연계되기 때문에 반응이 더욱 힘들다. 따라서 이산화탄소 전환효율을 증가시키기 위해 다양한 밴드위치를 가진 반도체 물질을 조합하여 효과적인 광전자생성을 유도하고, 도핑 및 광 흡수제를 이용한 빛 흡수율 증가, 조촉매 및 표면처리를 이용한 촉매활성 증가와 같은 다양한 개념들이 적용되었다.

1979년 혼다와 이노우에는 산화물과 비산화물 나노입자를 용액에 분산시켜 이산화탄소를 다양한 탄소유도체롤 변환시키는 광촉매적 이산화탄소변환 연구를 최초로 게제하였다. 또한 그래첼교수 및 연구원들은 루테늄 및 산화루테늄을 염료로 사용하여 염료감응형 이산화탄소전환 실험을 최초로 시도하였다. 이에 따라, 본 석사학위논문은 반도체 나노입자와 TiO_2 촉매를 이용하여 이산화탄소(CO_2) 변환효율을 증가시키기 위한 융합형 광촉매 시스템을 연구하였다.

1. 탄소와 질소가 동시도핑 된 이산화티탄 나노튜브를 이용한 이산화탄소의 광촉매성 탄화수소연료로의 변환 (Photocatalytic Conversion of CO_2 gas to hydrocarbon fuel using Carbon and Nitrogen co-doped Sodium Titanate Nanotubes)

TiO_2는 자체의 높은 안정성과 촉매활성 때문에 광촉매 중 에서 가장 많이 연구되고 사용되는 물질 중 하나이다. 하지만 큰 밴드갭 에너지에 의해 자외선영역의 빛만 흡수할 수 있어 가시광영역의 흡수를 증가시키기 위한 많은 연구가 진행되고 있다. 대표적인 경우가 금속 또는 비금속원소를 도핑하는 것이다. 도핑을 통해 밴드갭 내에 추가적인 도핑레벨이 생성되고 이로 인해 밴드갭 에너지가 작아지는 효과를 볼 수 있다. 뿐만 아니라 나노섬유, 나노판, 나노튜브와

같은 층상형 구조도 구조적 안정성 및 흡수향상을 유도할 수 있다. 층상형 구조는 다양한 이점을 갖게 된다. 먼저 큰 표면적, 흡착률, 열·화학적 안정성뿐만 아니라 촉매활성 또한 향상되게 된다. 이러한 이유에 의해 본 연구에서는 먼저 이산화티탄 나노튜브(Sodium Titanate Nanotube, Na^+-TNT)를 수열방법을 이용하여 합성하고, 탄소와 질소를 동시에 도핑 시킴으로써 광촉매 활성을 향상시켰다.

제작된 촉매는 다양한 분석기기를 통해 그 특성을 평가하였다. XRD 패턴을 통해 10.2º 에서 나타나는 주 피크가 높은 각도로 이동될 뿐만 아니라 그 세기 또한 감소하는 것을 확인할 수 있었다. 이는 도핑에 의한 효과로 볼 수 있다. 도핑을 할 때, 탄소와 질소의 원료인 요소와 이산화티탄나노튜브(TNT)를 곱게 갈아 열처리 하게 되는데, 이 과정에서 요소가 분해 되며 수소이온이 생성된다. 이 수소이온은 TNT 의 격자를 공격하게 되고 이로 인해 결정성이 떨어지게 되며 부분적으로 꼬임현상(local shrinkage)이 나타나게 된다. 그리고 나머지 나타나는 회절 피크를 통해 TiO_2의 anatase 상과 일치한다는 것을 확인하였다.

또한 TEM, SEM 과 같은 전자현미경 사진을 통해 직접적으로 TNT 의 형성을 확인할 수 있었다. 직경이 약 13nm 정도되는 긴 튜브형태를 보여주고 있으며 서로 복잡하게 뭉쳐 다공성 구조를 갖고 있다. 광 흡수특성을 조사하기 위해 UV-VIS 흡수를 측정하였다. UV-VIS 그래프를 보면 기존의 TNT 는 약 360nm 부근에서 흡수가 급격히 감소한다. 이는 일반적인 TiO_2 나노입자의 흡수경향과 비슷하다. 하지만 탄소와 질소를 함께 도핑 하였을 때 그 도핑 양을 증가 시킬수록 점점 가시광 영역의 흡수가 증가하는 것을 확인할 수 있었다. 또한 Tauc 방정식을 이용하여 흡수그래프로부터 밴드갭에너지를 간단하게 유도할 수 있다. 이를 통해 밴드갭에너지 또한 도핑 양을 증가 시킬수록 점점 작아지는 것을 확인 하였다. 위에서 언급했던 것과 같이, 밴드갭 사이에 탄소나 질소에 의한 에너지레벨이 추가적으로 생성되며 가시광 흡수가 증가한다는 이론과 일치하는 결과이다. 그 다음, TNT 내에 삽입 되어있는 Na^+ 이온의 존재와 탄소와 질소의 도핑유무를 측정하기 위해 라만 분광분석법을 도입하였다. 라만 그래프에서 대표적으로 4 개의 피크가 나타났는데 이들은 Ti-O-M(M=Na or Ti) 진동밴드에 해당한다. 특히 가장 높은 진동수를 갖는 피크의 경우 도핑 양이 증가할수록 그 세기가 감소하는 것을 확인할 수 있는데 이는 수소이온에 의해 TNT 에 존재하는 Na^+이온이 교환되는 현상에 의해 나타나는 것이다. 또한 TEM,

SEM 에서 확인했던 다공성 구조를 직접적으로 확인하기 위해 N_2 흡·탈착 실험을 진행하였다. 실험을 통해 얻는 BET 비표면적의 경우, TNT 와 C,N-TNT 를 비교하였을 때, 큰 차이를 보이지 않았다. 이는 탄소와 질소를 도핑 하는 과정이 TNT 간의 조직시스템에 큰 영향을 주지 않는다는 것을 말해준다.

광전자분광법(XPS)은 시편 내에 존재하는 결합에너지를 측정함으로써, 정성 및 정량 분석이 가능하다는 장점을 갖고 있어, 특성분석에 많이 사용하는 분석방법이다. XPS 그래프를 통해 시편 내에 탄소, 산소, 질소, 티타늄, 나트륨이 존재한다는 것을 survey scan 을 통해 알 수 있으며, 특정 부분을 확대하여 보면 더 자세한 결합에너지를 확인할 수 있다. 질소의 경우, N 1s 스펙트럼을 통해 도핑 양을 증가시킬수록 N 1s 피크의 세기가 강해지는 것을 확인할 수 있다. 이는 곧 시편 내에 존재하는 N 의 양이 많아짐을 뜻한다. 탄소의 경우, C 1s 스펙트럼을 보면 도핑 양을 증가 시킬수록 약 288 eV 부근에서 피크가 생성된 후 세기가 점점 강해지는 것을 알 수 있다. 이는 곧 피크가 도핑 된 탄소에 해당하는 것을 알 수 있으며 Ti 금속과 C 와의 결합에 의해 탄소의 전자 밀도가 상대적으로 금속에게 빼앗겨 낮아지게 되고 이로 인해, 결합에너지가 높은 곳에 피크가 나타나는 것으로 생각할 수 있다. 티타늄 또한 일반적인 TiO_2 에서 보여지는 양상과 비슷한 피크를 보여준다. 이를 통해 주로 Ti 원소가 $TiO_2(Ti^{4+})$ 형태로 존재한다는 것을 알 수 있다. 산소의 경우도 마찬가지로 O 1s 스펙트럼에서 약 529 eV 에서 나타나는 피크가 일반적인 Ti-O 결합을 뜻하며 뒤에 추가적으로 나타나는 피크는 이중결합산소에 의해 나타나는 피크이다.

이렇게 구조분석을 마치고, 광 활성을 측정하기 위해 염료 분해 실험과 이산화탄소전환 실험을 진행하였다. 이 모든 실험은 태양에서 나오는 빛과 같은 조성을 같은 빛을 만들어낼 수 있는 솔라시뮬레이터를 이용하여 진행하였다. 먼저 이산화탄소전환 실험이 기체상에서 진행 되었다. 준비된 촉매를 반응기 내에 위치하고 내부를 오직 이산화탄소와 수증기로만 채워준 후, 빛을 조사하여 생성되는 생성물을 가스크로마토그램(GC)을 통해 분석하였다. GC 에서 측정된 자료를 정량분석을 통해 생성량을 계산하게 되면 위의 이산화탄소전환률 그래프를 얻을 수 있다. C,N-TNT01 의 경우 일반적인 경향에서 약간 벗어나는 것을 볼 수 있으나 오차범위 내에 위치한다고 할 수 있다. 그 이외에 C,N-TNT06 이 가장 높은 이산화탄소변환률을 보여주었으며, 한 시간 동안

빛을 조사하였을 때 생성된 양은 약 9.75 μmol/g 으로 순수한 TNT 보다 약 2.5 배 높은 값이다. 이를 통해 이산화탄소 전환실험에서 C,N-TNT06 이 가장 최적화 되어있는 조건이라고 할 수 있다. 반면에 염료 분해 실험에서는 이전과는 다른 실험양상을 보여주었다. 약 두 시간 동안 빛을 조사하면서 20 분 간격으로 시편을 추출하여 흡광도를 분석해보았다. 데이터에서 볼 수 있듯이 도핑 양이 증가할수록 분해되는 속도 또한 지속적으로 증가하였다. 대략 58% 의 염료가 C,N-TNT1 에 의해 2 시간동안 분해 되었으며 순수한 TNT 가 같은 조건하에서 30% 이하를 분해한 것과 비교하였을 때 약 2 배정도 향상된 촉매활성을 갖고 있다고 볼 수 있다. 실제로 분해되기 전과 후의 농도를 이용하여 반응속도상수를 계산하여 비교한 결과, C,N-TNT1 의 속도상수가 순수한 TNT 보다 약 2.5 배 빠르다는 것이 확인 되었다. 이는 결국, 위에서 언급한 것과 마찬가지로 탄소와 질소의 동시도핑에 의해, 가시광 영역에서 빛의 흡수가 증가하게 되고 이로 인해 더 많은 광전자가 생성되게 된다. 이렇게 생성된 광전자는 표면으로 이동하여 분해 반응에 참여하게 되고 분해효율이 증가하게 되는 것이다.

이산화탄소 전환에 대한 메커니즘도 이와 비슷하게 작용한다. 탄소와 질소의 동시도핑에 의해 광전자의 양이 많아지며 이로 인해 많은 활성부위가 나타나게 된다. 이곳에서 정공은 물과 만나 산소와 수소이온을 생성하게 되고, 전자는 표면에 흡착된 이산화탄소 분자와 수소이온과 만나 메탄 및 유기물을 생성하게 된다. 효율 향상에는 단순히 가시광 흡수뿐만 아니라 조금이지만 표면적의 향상과 밴드갭의 최적화 등과 같은 다양한 요소가 복합적으로 관계되어 있다.

요약하자면, 이산화티탄 나노튜브와 이에 탄소와 질소의 동시도핑이 수열방법과 열처리 과정에 의해 쉽고 간단하게 제작되었으며, 이렇게 제작된 촉매는 다양한 분석기기, 예를 들면 TEM, SEM, XRD, Raman 를 이용하여 특성분석 되었다. 또한 광촉매적 이산화탄소전환 실험, 염료 분해 실험을 통해, 제작된 촉매의 광촉매 특성을 평가하였다. 탄소와 질소를 동시 도핑하면서 가시광 영역의 빛의 흡수가 증가하였으며 이는 도핑에 의한 밴드갭 내의 추가적인 에너지레벨 생성에 의해 나타난 현상이다. 광촉매 특성 또한 도핑과 함께 그 효율 또한 증가하는 것을 확인할 수 있었으며, 이는 표면적 및 가시광 영역의 빛 흡수 증가와 구조적 특성에 의한 효율적인 전자와 정공의 분리에 의해 나타난 현상이라고 볼 수 있다.

2. 태양광 아래 이산화탄소의 광촉매적 환원을 위한 헤테로 구조를 융합형 지닌 산화구리-염소도핑 이산화티탄 복합체의 연구 (Hybrid CuO-$TiO_{2-x}Cl_x$ Hetero structured composites for CO_2 reduction by simulated Solar Irradiation)

위에서 언급하였듯이, TiO_2는 가장 많이 사용하는 촉매물질 중 하나 이지만 가시광 영역의 흡수가 어려워 이를 해결하기 위한 많은 연구가 진행되고 있다. 비금속 원소의 도핑이 많이 연구되고 있으나 그 중에서도 할로겐 계열 원소의 도핑에 대한 연구는 아직 미비한 수준이다. 그 이유는 할로겐 계열의 원소는 불소를 제외하고 나머지 원소인, 염소, 브롬, 요오드의 경우 산소보다 이온크기가 크기 때문에 도핑이 힘들기 때문이다. 하지만 이론적인 계산에 의해서 할로겐 계열의 원소를 도핑 하였을 경우, 일반적인 탄소나 질소 같은 비금속 원소 보다 더 높은 활성을 가질 수 있다고 연구한 논문이 있다.

이산화티탄의 단점을 극복하기 위한 또 다른 전략은 바로 작은 밴드갭을 가진 반도체 물질을 함께 적용하는 것이다. 작은 밴드갭을 가진 반도체 물질은 다양하게 존재하는데 주로 PbS, CdSe, CuO 등이 있다. 이러한 물질은 나노입자로 만들 경우 가시광 영역의 빛을 흡수할 수 있을 뿐만 아닐 적외선 영역의 빛 또한 흡수 할 수 있으며 선택적으로 제작할 수 있어 큰 이점을 갖고 있다. 이 중에서 CuO가 이산화탄소전환 촉매로서 전망을 갖고 있다고 말할 수 있다. CuO는 p형 반도체로써, 약 1.3~1.5 eV의 밴드갭을 갖는다. 그리고 밸런스밴드에너지레벨이 CO_2 변환레벨과 비슷한 위치에 존재하고 있을 뿐만 아니라 이산화탄소 흡착에 대해 특이성을 갖는 특성이 알려지면서 이산화탄소 전환촉매에 응용되기 시작하였다.

본 연구에서는 위 두 가지 개념을 복합적으로 도입하여, 산화구리와 염소 도핑 이산화티탄을 이용하여 헤테로구조의 촉매를 합성하여 이산화탄소 전환 연구에 활용하였다. 합성의 첫 번째 과정으로 Cu/Cu_2O 나노입자를 열침전법을 이용하여 준비한다. 이렇게 준비된 나노입자와 사염화티타늄을 비극성 용매에서 반응을 시켜 헤테로 구조의 복합체를 얻게 된다. 공기 중에서 자연스럽게 산화를 시키며 염소가 TiO_2 내에 도핑이 되고 나머지 염소는 염소산화물로써 표면에 남아있게 된다.

먼저 균일한 크기분포를 갖는 Cu/Cu_2O 나노입자를 합성해야 한다. TEM 과 HR-TEM 이미지를 통해 나노입자가 약 14nm 의 크기를 갖고 균질 하게 분포해 있는 것을 확인 할 수 있었으며, 내부는 순수한 구리(Cu), 외부는 아산화구리(Cu_2O) 로 이루어져 있는 것을 표면 격자 간격을 통해 알 수 있었다. 이러한 결과는 XRD 패턴과도 일치한다. XRD 패턴에서 주로 순수 구리에 대한 패턴이 확인 되었으며 작은 세기의 Cu_2O에 대한 피크가 확인 되었다. 흡수 또한 상당이 날카로운 모양의 흡수 피크를 보여주었다. 이는 곧 일정한 크기분포를 지니고 있다는 것을 의미하며, Cu/Cu_2O 나노입자의 표면 플라즈몬효과에 의해 나타나는 흡수피크임을 알 수 있다.

TEM 이미지를 통해, 준비한 시편이 헤테로구조의 복합적인 형태를 띄고 있다는 것을 확인하였으며, HR-TEM 이미지를 통해 TiO_2와 산화구리가 시편 내에 존재한다는 것을 격자간격을 통해 알 수 있었으며, TiO_2 표면에 산화구리 입자가 붙어 있는 형태를 갖고 있다는 것을 확인하였다. 이러한 접촉계면에서 p-n 접합이 형성되게 되며 이를 통해 전자와 정공의 분리가 더 효과적으로 나타날 것이다. 또한 이미지 내부에 존재하는 SAED 회절패턴을 통해 TiO_2 와 산화구리가 존재한다는 것을 확신할 수 있었다.

제작된 시편의 광 흡수특성을 평가하기 위해 흡수분광기를 도입하였다. 흡수그래프에서 CT03, 05, 07, 09 로 시편을 표시하였는데 뒤의 숫자는 일정한 양의 Cu/Cu_2O 나노입자 용액에 들어간 사염화티타늄의 양을 뜻한다. 흡수그래프를 보면 400~500 nm 부근 과 800 nm 부근에서 넓은 흡수분포를 갖고 있다. 400nm 부근의 흡수는 일반적인 TiO_2에 의한 자외선영역의 흡수를 의미한다. 산화구리를 도입하고 염소의 도핑 하였을 때, 400 nm에서 조금 긴 파장 쪽으로 흡수밴드가 이동하고 범위 또한 조금씩 증가하는 것을 확인 할 수 있다. 이는 산화구리의 산소에서 구리로의 전하이동에 의한 흡수피크로서 상대적인 산화구리의 양이 증가함에 따라 흡수세기 또한 증가하는 것을 볼 수 있다. 하지만 염소를 도핑 하였을 경우에도 400 nm 부근에서 흡수밴드의 이동이 나타나고 가시광 흡수가 증가하는 것이 이전에 연구된 논문을 통해 증명되었기 때문에, 지금 나타난 흡수양상은 산화구리와 염소도핑에 대한 효과가 섞여서 나타났을 가능성이 높다. 따라서 정확히 구분하기가 힘들다고 말할 수 있다. 긴 파장 영역에서 나타나는

광범위한 흡수는 산화구리에 의해 나타나는 흡수이다. 이는 산화구리의 d-d 전이에 의해 나타나는 흡수로서 전형적인 산화구리 패턴을 뜻한다.

XRD 패턴 분석에서는 일반적인 TiO_2, 산화구리와 제작된 시편을 비교하였을 때, 큰 차이가 없음을 알 수 있다. 왜냐하면 산화구리의 경우 TiO_2에 비해 상대적으로 소량이 함유되어 있기 때문에 산화구리의 피크가 TiO_2 피크의 세기에 묻혀 확인 할 수 가 없다. 또한 염소가 도핑 되었을 경우, 몇몇 논문은 TiO_2 피크가 낮은 각도 쪽으로 약간 이동한다고 설명하였으나, 그 값이 너무 미비하여 구분하기 힘들다.

하지만 광전자분석법(XPS)를 통해, 시편 내에 존재하는 원소를 분석할 수 있었다. Cu 2p 의 경우 위성피크는 산화구리에서만 나타나는 고유피크 인데, 제작된 시편에서 위성피크가 나타나는 것으로 보아 구리가 산화구리의 형태로 존재한다는 것을 유추 할 수 있었다. O 1s 또한 CuO 와 TiO_2, 그리고 표면 오염에 의한 피크까지 세 개로 나누어지는 것을 확인할 수 있었고, Cl 2p는 크게 두 개로 나누어지는 것을 확인할 수 있었다. 첫 번째 낮은 에너지에서 나타나는 피크의 경우 도핑 된 염소에 대한 피크이며 두 번째 피크의 경우 염소산화물에 해당한다. 이를 통해 염소가 TiO_2 내에 도핑 되었으며 표면은 염소산화물이 존재한다는 것을 알 수 있다.

제작된 시편의 광촉매 특성을 확인하기 위해 이산화탄소 전환실험과 광전류 측정 실험을 수행하였다. 또한 시편의 촉매활성을 비교하기 위해 순수한 산화구리와 TiO_2를 사용하였다. 1시간동안 이루어진 광촉매 반응에 의해 생성되는 주 생성물은 메탄이며 부산물로써 소량의 에탄 또한 검출 되었다. 하지만 도표상에는 메탄만 표시하였다. 산화구리와 염소도핑 Ti02가 함께 사용되었을 때 급격한 효율의 향상을 볼 수 있다. CT07의 경우 순수한 산화구리에 비해 약 10배, TiO_2에 비해 약 22배 정도 생성률이 향상되었다. 이를 통해 적절한 조건에서 p-n 접합에 의한 효과와 도핑, 그리고 산화구리에 의한 가시광 영역의 활성에 의해 효율이 급격히 증가했다고 볼 수 있다. 제작된 시편이 표면에 존재하는 탄소 오염원 때문이 아닌 인위적으로 주입해준 이산화탄소에 의해서만 촉매활성을 갖는다는 것을 확인하기 위해, 순수한 Ar 분위기에서 측정한 결과값을 함께 사용하였다. Ar 분위기 상에서 광촉매 반응에 의한 메탄은 거의 검출되지

않았으며 이 결과를 통해 메탄이 오직 대기중의 이산화탄소에 의해서만 생성되었다는 것을 확신할 수 있었다.

제작된 시편의 광 반응성을 평가하기 위해 광전류를 측정하였다. 광촉매 실험과 같은 조건의 빛을 사용하였으며, CT07을 대상으로 측정하였다. 또한 비교 군으로 CuO 와 TiO_2을 물리적으로 섞어 측정함으로써, p-n 접합의 효과를 확인하고자 하였다. 실험 결과를 보면, CT07이 물리적으로 준비한 것보다 약 3배 정도 높은 광전류를 보여주었다. 비록 광 안정성은 30% 정도 감소하였지만 이를 통해 p-n 접합이 성공적으로 구현되었으며 높은 전하 수집률을 보여준다는 것을 확인할 수 있었다.

결론적으로, 에너지 부족현상 및 환경오염등과 같은 문제 때문에 대체 에너지에 대한 수요가 증가함에 따라, 광화학적 이산화탄소 환원연구는 이러한 수요를 충족시킬 수 있는 촉망 받는 연구분야 중 하나이다. 따라서 이 논문은 반도체 나노입자와 이산화티탄 촉매를 이용하여 이산화탄소(CO_2) 변환효율을 증가시키기 위한 융합형 광촉매 시스템에 대한 연구이다.

먼저, 탄소와 질소가 함께 도핑 된 이산화티탄 나노튜브 (C,N-TNT) 가 수열방법과 소성과정을 통해 성공적으로 합성되었다. C,N-TNT 의 광촉매적 특성은 염료분해 실험과 이산화탄소 환원을 인공 태양빛 아래에서 평가되었다. C,N-TNT1 (Urea/TiO_2=10) 염료분해 실험에서 가장 빠른 분해속도를 보여주었으나, 이산화탄소 환원에서는 C,N-TNT06 이 가장 빠른 메탄생성속도를 보여주었다. 또한 헤테로구조를 지닌 산화구리-염소도핑 이산화티탄 ($CuO-TiO_{2-x}Cl_x$) 복합체가 새로운 실험 방법을 통해 성공적으로 합성 되었으며, 이 촉매에 대한 광촉매 특성이 기체크로마토그램(GC)을 이용한 이산화탄소 전환 실험을 통해 평가 되었다. 이산화탄소 전환효율을 증가 시키기 위한 실험적 전략은 산화구리(CuO) 와 염소가 도핑된 이산화티탄 (Cl doped TiO_2)을 함께 사용하는 것이다. 이렇게 하여 만들어진 p-n 접합구조는 광유발 전자 및 정공의 분리에 큰 효과가 있다. CT07 을 다른 촉매와 비교하였을 때, 급격히 향상된 이산화탄소 전환 활성을 보여주었다.

핵심어: 탄소와 질소가 동시 도핑된 이산화티타늄 나노튜브, 염소 도핑 이산화티타늄, 산화구리, p-n 헤테로접합, 광촉매적 이산화탄소 환원